NASA CR-135391
R77AEG400

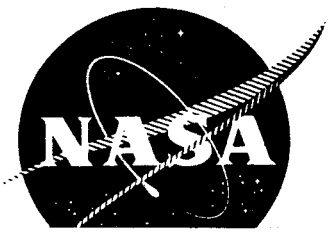

(NASA-CR-135391) CORE COMPRESSOR EXIT STAGE STUDY. VOLUME 1: BLADING DESIGN Design Report, Oct. 1976 - Apr. 1977 (General Electric Co.) 67 p HC A04/MF A01 CSCL 21E

N78-29099

Unclas
G3/07 25139

CORE COMPRESSOR EXIT STAGE STUDY

Volume I - Blading Design

by

D.C. Wisler

General Electric Company
Aircraft Engine Group
Cincinnati, Ohio 45215

Prepared For

National Aeronautics and Space Administration

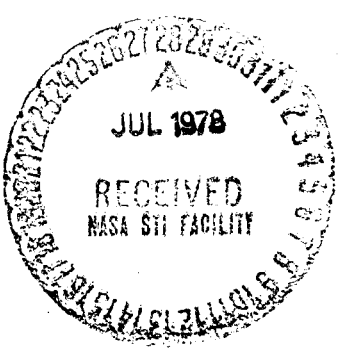

December 1977

NASA Lewis Research Center
Contract NAS3-20070

This is the Design Report on

Core Compressor Exit Stage Study

Contract NAS3-20070

Is your mailing address correct?

If not, please notify NASA Project Manager, Item #15 on the first page.

1. Report No.	2. Government Accession No.	3. Recipient's Catalog No.
NASA CR-135391		

4. Title and Subtitle	5. Report Date
Core Compressor Exit Stage Study Volume I - Blading Design	December 1977
	6. Performing Organization Code
7. Author(s)	8. Performing Organization Report No.
D.C. Wisler	R77AEG400
	10. Work Unit No.
9. Performing Organization Name and Address	
General Electric Company Aircraft Engine Group Cincinnati, Ohio 45215	11. Contract or Grant No. NAS3-20070
	13. Type of Report and Period Covered Design Report, October 1976 - April 1977
12. Sponsoring Agency Name and Address	
National Aeronautics and Space Administration Washington, D. C. 20546	14. Sponsoring Agency Code

15. Supplementary Notes

Project Manager, Dr. Wojciech Rostafinski, Fluid System Components Division, NASA-Lewis Research Center, Cleveland, Ohio 44135

16. Abstract

This report describes the design of a baseline compressor test stage and the design of a candidate rotor and two candidate stators that have the potential of reducing endwall losses relative to the baseline stage. These test stages are typical of those required in the rear stages of advanced, highly-loaded core compressors. The baseline Stage A is a low-speed model of Stage 7 of the 10-stage AMAC compressor whose preliminary design was identified in a previous study. Candidate Rotor B uses a type of meanline in the tip region that unloads the leading edge and loads the trailing edge relative to the baseline Rotor A design. Candidate Stator B embodies twist gradients in the endwall region. Candidate Stator C embodies airfoil sections near the endwalls that have reduced trailing edge loading relative to Stator A. The overall technical approach for the program will utilize the General Electric Low Speed Research Compressor as the principal investigative tool. Tests will be conducted using four identical stages of blading so that the designs described in this report will operate in a true multistage environment.

17. Key Words (Suggested by Author(s))	18. Distribution Statement
Compressor Core Compressor Design Report	Unclassified - Unlimited

19. Security Classif. (of this report)	20. Security Classif. (of this page)	21. No. of Pages	22. Price*
Unclassified	Unclassified	59	

* For sale by the National Technical Information Service, Springfield, Virginia 22151

TABLE OF CONTENTS

LIST OF TABLES

LIST OF ILLUSTRATIONS

LIST OF ILLUSTRATIONS (Continued)

LIST OF ILLUSTRATIONS (Concluded)

LIST OF SYMBOLS

Symbol	Definition
C	Chord
D	Diffusion Factor
i	Incidence Angle
M	Mach Number (primed quantities denote relative frame)
P	Pressure
$\underline{P}$	Average Pressure
$\overline{P}(\psi)$	Pressure at a Particular Streamline Location
r	Radius
t_{max}	Maximum Thickness
t_{te}	Trailing Edge Thickness
U	Wheel Speed
V	Air Velocity (primed quantities denote relative frame)
Xp	Blade Design Experience Factor Described in Section 5.0
β	Air Angle (primed quantities denote relative frame)
β^*	Airfoil Meanline Angle
δ	Deviation Angle
ζ	Stagger Angle
σ	Solidity
ϕ	Camber
ω	Loss Coefficient

Subscripts

P	Pitchline Location
S	Static Properties
T	Total Properties
Z	Axial Direction
θ	Tangential Direction
1	Blade or Vane Inlet
2	Blade or Vane Exit

1.0 SUMMARY

The Core Compressor Exit Stage Study Program has the primary objective of developing rear stage blade designs that have improved efficiency by virtue of having lower losses in their endwall boundary layer regions. Blading concepts that offer promise of reducing endwall losses will be evaluated in the multistage environment. This report describes the aerodynamic design of the baseline compressor test stage and the design of a candidate rotor and two candidate stators that have the potential of reducing endwall losses relative to the baseline design. These test stages are typical of those required in the rear stages of advanced, highly-loaded core compressors. Testing will be conducted in the General Electric Low Speed Research Compressor which incorporates four identical stages to achieve a multistage environment.

The baseline Stage A is a low-speed model of the seventh stage of the 10-stage, 23:1 pressure ratio AMAC study compressor whose preliminary design study was conducted under NASA Contract NAS3-19444. The low speed modeling was accomplished by modifying the camber line of the low-speed airfoil sections so that the dimensionless suction surface velocity distributions of the low speed sections were similar to those of Stage 7 of the AMAC compressor. The Baseline Rotor A consists of airfoil sections having modified circular arc meanlines and circular arc thickness distributions. The baseline Stator A consists of airfoil sections having a 65-series thickness distribution on modified circle arc meanlines. An IGV was designed which gave the required preswirl to the fluid entering the first rotor in order to achieve a multistage environment in as few stages as practical. Standard General Electric IGV design practices were employed.

Rotor B, Stator B and Stator C are candidate designs that have the potential of reducing endwall losses relative to the baseline Stage A. Rotor B was designed to the same set of vector diagrams as Rotor A, but uses a type of meanline in the tip region that unloads the leading edge and loads the trailing edge relative to Rotor A. Recent low-speed test results indicate that very small rotor wakes are present in the tip region of rotors similar in design to Rotor A. This region should, therefore, be able to take higher trailing edge loading without undue risk of separation. The modification to the tip region was blended into the pitchline so that Rotor A and Rotor B were identical from the pitchline to the hub.

Stator B embodies blade sections twisted closed locally in the endwall regions similar to those used in a highly loaded NASA single stage that had rather good performance for its loading level. Different vector diagrams were calculated to account for the high values of swirl angle near the endwalls. The appearance of Stator B is quite different from that of Stator A because of the twist gradients and because the vane was stacked at 30 percent chord from the leading edge in order to reduce the leading edge lean angle.

Stator C embodies airfoil sections near the endwalls that have reduced trailing edge loading and increased leading edge loading relative to Stator A. The airfoils were designed to the same vector diagram as Stator A.

2.0 INTRODUCTION

Recent preliminary design studies of advanced turbofan core compressors (Reference 1) have indicated that such compressors must have very high efficiencies, as well as the advantages of compactness, lightweight and low cost, in order for advanced overall engine/aircraft systems to have an improved economic payoff. Loss mechanism assessments, such as that of Reference 2, suggest that approximately half of the total loss in a multistage compressor rear stage is associated with the endwall boundary layers. Since only a relatively small amount of past research has been dedicated to the problem of finding improved airfoil shapes for operation in multistage compressor endwall boundary layers, it is believed that substantial improvements in that area are likely. Accordingly, a goal of a 15 percent reduction in rear stage endwall boundary layer losses, compared to current technology levels, has been set. The Core Compressor Exit Stage Study program is directed at achieving this goal. Blading concepts that offer promise of reducing endwall losses will be evaluated in a multistage environment. The design of this blading is described in this report.

3.0 LOW SPEED MODELING AND TESTING CONCEPT

The blading designed for the Core Compressor Exit Stage Study Program is basically a low-speed model of a rear stage of the high-speed AMAC compressor described in Reference 1. This low-speed model will be tested in the General Electric Low Speed Research Compressor. A cross-section of this facility is shown in Figure 1. In order to properly simulate loss mechanisms and establish a true multistage environment, four identical stages will be employed. The third stage will be the test stage.

The principal advantage offered by the low-speed testing approach is that the large size (1.5 m diameter) and low tip speed (60 m/sec) of this test rig enables very detailed data to be obtained without risk of instrumentation blockage effects, which in turn enables precise identification of where and how aerodynamic losses originate. It is very difficult to determine these losses in a high-speed core compressor where rear stage blade heights may be quite small. In smaller, higher-speed compressors with closely spaced blades, the number of radial and circumferential samples of the flow is necessarily limited, and there is no possibility of obtaining blade surface pressure distributions or of visually observing the flow field with tuft probes, as can be done in a low-speed test rig.

The low-speed testing approach is, of course, only appropriate if there is confidence that the results will not be misleading. Fundamental fluid dynamic principles and reasoning support the low-speed modeling approach as long as certain limitations are observed. Airfoil surface velocity distributions must be similar in order for the high and low-speed bladings to have similar boundary layers and loss regions. Compressible cascade analysis procedures have been successfully used for this purpose by General Electric in previous programs, and it has been found that the small differences in blade geometry needed to model the dimensionless suction surface velocity distribution of a high-speed blade with an equivalent low-speed airfoil can be conveniently defined using such an analysis technique. The low-speed modeling approach cannot simulate airfoils having shocks on their surface, but this is not an issue in core compressor rear stages. It is also necessary that the Reynolds number should be reasonably close to that of the high-speed blading so that the turbulent/laminar characteristics of the flow are modeled. Here, the large size of the Low Speed Research Compressor is helpful; with chord lengths of about 9 cm that result from use of a radius ratio of 0.85 and an aspect ratio of 1.2, the blade chord Reynolds number is about 360,000. This is approximately half that existing in high-speed compressors operating at subsonic altitude cruise conditions and is close enough to provide a proper simulation.

Some results previously obtained from the Low Speed Research Compressor are presented in References 3 and 4. These are believed to be in good agreement with high-speed results.

4.0 PRELIMINARY DESIGN OF NASA/GE AMAC COMPRESSOR AND LOW SPEED MODEL

AMAC Compressor Design

A preliminary design study program, which identified an advanced core compressor for use in new high-bypass ratio turbofan engines to be introduced into commercial service in the 1980's, was previously conducted and is described in Reference 1. The selected compressor design, called the AMAC (Advanced Multistage Axial-Flow Compressor) compressor, was a 10-stage 23:1 pressure ratio compressor offering the best combination of the following advantages: high efficiency, low operating cost, low fuel usage, and acceptable development risk. A flowpath of the AMAC compressor is shown in Figure 2 and its design parameters are given in Table 1.

Stage 7 of the AMAC compressor was chosen as a typical rear stage for low speed modeling. Design data for Stage 7 are presented in Table 2 and in Figures 3 through 8 together with data for Stage A, its low-speed model. As seen in Figure 3, a radially nonconstant distribution of total pressure at the rotor exit has been employed. For graphical presentation, the average total pressure at the exit plane is subtracted from this value and the result is normalized by the local pitchline dynamic head at the stage inlet. The selected profile is linear with a somewhat higher-than-average value near the hub and a somewhat lower-than-average value near the tip. The higher hub total pressure increases the dynamic head entering the stator vanes in this region and helps avoid excessive loading. The radial distributions of loss coefficient are shown in Figure 4. These distributions are consistent with General Electric experience for advanced, highly loaded core compressors. The stator exit swirl angles shown in Figure 5 were specified, and the stator inlet angles shown resulted from vector diagram calculations. The resulting rotor inlet and exit relative air angles are presented in Figure 6. Since the value of the relative air angle is strongly dependent upon blade speed, the ordinate of Figure 6 is presented as local radius divided by pitchline radius in order to demonstrate the good agreement between Rotor 7 and Rotor A vector diagrams in the pitchline region. The radial distributions of normalized axial velocity at the rotor inlet and exit planes are shown in Figure 7. Finally, the radial variations in rotor and stator diffusion factors are presented in Figure 8.

Analysis of Low Speed Stage A Vector Diagrams

Stage A was designed to be a low-speed model of the AMAC Stage 7. In order to utilize existing hardware, the low speed configuration was designed to have a radius ratio of 0.85 rather than the 0.89 value of Stage 7. It is believed that once the radius ratio becomes high enough that significant radial imbalances in loading are unlikely, the radius itself ceases to be a significant dimensionless variable. The significant parameters are then aspect ratio, solidity, clearance/blade height, axial blade row spacing/chord

and vector diagram quantities, such as the flow and pressure-rise coefficients. Therefore, if these parameters are modeled in the 0.85 radius ratio rig, the data obtained in these tests may be applied directly to higher radius ratio stages without any adjustment for radius ratio per se.

A vector diagram analysis for Stage A was conducted using rotor exit total pressure, loss coefficient, and stator exit swirl angle profiles that were essentially identical to those of AMAC Stage 7 (Figures 3 through 5). These profiles, along with the Low Speed Research Compressor annulus dimensions, an effective area coefficient of 0.95, rotative speed, and an airflow that closely matched the axial velocity/blade speed ratio of Stage 7, were input into the CAFD computer.* The results of the Stage A vector diagram analysis are compared to those for Stage 7 in Tables 2 and 3 and in Figures 3 through 8, all of which were referred to previously. The radial variation of normalized inlet total pressure, shown in Figure 3, is nearly identical for the two cases. As can be seen in Figure 6, the low-speed model requires approximately 1.9 degrees more rotor turning than the high-speed design in order to obtain comparable rotor diffusion factors (needed to obtain similar blade surface velocity distributions) in the incompressible case where the axial velocity ratio is 1.0. The high-speed compressor, on the other hand, gains part of its blade loading from a reduction in axial velocity, as is shown in Figure 7. Rotor and stator diffusion factors, compared in Figure 8, are modeled reasonably well. All other vector diagram parameters can be modeled quite well. As seen in Table 2, blade solidity and aspect ratio can be closely modeled within the limitations imposed on numbers of blades and vanes and on axial stage length that arise through the use of existing hardware. The Stage A reaction is 0.628 and the Reynolds number is 360,000. This Reynolds number is substantially above the critical values that are sometimes encountered in compressor performance testing.

The vector diagram information presented for Stage A was also used to design Rotor B and Stator C. The vector diagram analysis for Stator B is presented in the following section.

Analysis of Low Speed Stator B Vector Diagrams

Stator B embodies twist gradients in the blade endwall region similar to those used in a highly loaded single stage, described in Reference 6, that had good performance for its loading level. The design goal for Stator B was to incorporate twist in the blade endwall region, while maintaining the same pressure rise, flow coefficient and average stator exit tangential momentum as in Stage A. This was accomplished by using an iterative CAFD analysis in which the radial distribution of Stator B exit swirl angle was varied until:

*The Circumferential-Average Flow Determination (CAFD) computer program provides a numerical solution of the radial-equilibrium equation, continuity equation, energy equation, and equation of state, including the effects of gradients of entropy and enthalpy. A derivation of the equations is given in Reference 5.

(1) the desired twist was incorporated into the endwall region of the vane and, (2) the average stator exit tangential momentum of Stage B was equal to that of Stage A. The CAFD analysis for Stator B provided vector diagram and loading information as shown in Table 4 and in Figures 9 through 12. The CAFD analysis was conducted as if a new rotor were being designed for Stator B, since it was initially thought that a new rotor might be needed to match the Stator B vector diagrams. However, a comparison of the relative air angles in Figure 10 indicates that the rotor angles required with Stator B are close enough to those of the Rotor A design that new rotor blading was not justified for such small and localized differences near the endwalls.

Although Stator B is twisted closed about eight degrees in the endwall regions, the flow turning in Stator B is nearly identical to that in Stator A at all immersions. Stator B exhibits lower values of axial velocity than Stator A in the endwall region and higher values in the pitchline region as seen in Figure 11. This same radial redistribution of the flow leads to higher predicted values of endwall rotor diffusion factors and lower predicted values of pitchline rotor diffusion factors as shown in Figure 12. Stator B diffusion factors, also shown in Figure 12, are nearly the same as those for Stator A.

5.0 BLADE SETTING PROCEDURE

The airfoil sections designed for the Core Compressor Exit Stage Study Program were specified to match the vector diagrams described in Section 4.0. The rotor airfoil sections consisted of modified circular arc meanlines with double-circular-arc-type thickness distributions. The stator airfoil sections consisted of modified circular-arc meanlines with 65-series thickness distributions. The modifications to the circular-arc meanlines were necessary in order to model the high-speed blading, i.e., to achieve the same suction surface velocity distributions for the candidate rotor and stator designs.

Incidence Angle

The leading edge meanline angles for AMAC Stage 7 were determined by utilizing the General Electric Smooth-Flow Incidence Angle Correlation. The "smooth-flow" incidence angle is defined as the incidence angle in potential flow through a two-dimensional cascade for which the stagnation streamline attaches directly to the leading edge point of the airfoil. Selection of this angle avoids high velocities on the suction surface in the leading region. It represents the angle for which the losses should be near minimum. In this correlation the "smooth-flow" incidence angle is related to the cascade geometry for airfoils with circular-arc meanlines. For the low-speed stages of this study, incidence angles were selected either to model the velocity distributions of Stage 7 or to achieve a defined departure from them, as will be explained in Sections 6 through 9.

Deviation Angle

The deviation angle was obtained by applying a potential flow cascade analysis (CASC) procedure to establish the required trailing edge metal angle, rather than the more conventional design method of using Carter's Rule. This was done primarily because Carter's Rule is usually applied to circular-arc meanlines and the meanlines used in this program differ from a circular-arc. A more accurate and general procedure was thus required. This procedure is described as follows.

The Cascade Analysis by Streamline Curvature (CASC) computer program is General Electric's primary blade-to-blade analysis tool. The CASC program solves the momentum and continuity equations in intrinsic coordinates to obtain the flow properties at the orthogonal-streamline intersections. In order to use the CASC program, however, it is necessary to determine the potential flow cascade exit air angle, β_{CASC}, that the blade must be designed to achieve. This angle is different from the CAFD exit air angle, β_{CAFD}, described in Section 4.0. It is the angle obtained after viscous wakes have been mixed out, after the effects of uncambering due to thick

suction surface boundary layers have been incorporated and after endwall effects have been included. The difference between these two angles is expressed as X_p in equation (1).

$$X_p \equiv \beta_{CAFD} - \beta_{CASC} \quad (1)$$

This difference, shown in Figure 13 for Stage A, was determined from a detailed data match/analysis using test data from a previous Low Speed Research Compressor program which had blading somewhat similar to that of Stage A. The radial distribution of CASC potential flow exit air angles was determined from the CAFD exit air angles shown in Figures 5 and 6 by using equation (1) and the radial distribution of X_p shown in Figure 13.

An inviscid secondary flow analysis was conducted for Stage A. The calculated cross-passage components yield an overturning (or underturning) of the flow going through each blade row relative to the turning given by ordinary cascade calculations or cascade data. Comparing the radial distribution of X_p shown in Figure 13 with the amount of overturning (underturning) predicted for Stage A by the secondary flow analysis indicates that secondary flow calculations can explain most of the X_p. Apparently, a large part of the empirical X-factor can be handled theoretically, and the portion caused by viscous effects may be relatively small in many cases.

The following iterative technique was then used to determine deviation angle: (1) a trial airfoil trailing edge meanline angle was chosen which established a trial airfoil shape; (2) a CASC analysis was conducted using the trial airfoil geometry and the potential flow cascade air angle obtained above; (3) the CASC solution was examined to determine whether the Kutta condition was satisfied at the trailing edge; and (4) the above three steps were repeated until the Kutta condition was satisfied. This CASC analysis also yielded airfoil surface velocity distributions which were used in the design of the airfoil shapes.

Meanline Modifications

Modifications to a circular-arc meanline were necessary in order to model the high speed blading and in order to achieve the desired surface velocity distributions for candidate rotor and stator designs. These modifications were accomplished by either overcambering or undercambering the airfoil in the leading edge and/or trailing edge region. The computer technique used is described as follows for an airfoil which is to have overcambering in the leading edge region relative to a circular-arc meanline. Values of input leading and trailing edge meanline angles are specified together with the amount of leading edge overcambering, ΔCAM_{LE}, and the blend point along the chord where the overcambered region blends into the circular arc region. The specified amount of ΔCAM is subtracted from the input value of leading edge meanline angle to obtain a new "reduced" value of leading edge meanline angle. A circular-arc distribution of meanline angle versus

percent chord is then constructed between the "reduced" leading edge meanline angle and the input trailing edge meanline angle. This circular-arc distribution is modified by blending a cubic curve from the specified blend point on the circular-arc distribution to the original input value of leading edge meanline angle, resulting in a meanline that has more camber in the leading edge region than a circular-arc. Undercamber is accomplished by simply changing the sign of ΔCAM. Modifications of the trailing edge region are treated in essentially the same manner. A wide variety of loading distributions can be achieved by varying the amount of ΔCAM, the blend point and the location of maximum airfoil thickness.

6.0 DESIGN OF STAGE 7/STAGE A

Stage 7 of the 10-stage, 23:1 pressure ratio AMAC study compressor was selected as a typical rear stage of an advanced highly loaded core compressor. Stage A, the low speed baseline model of Stage 7, was designed to have dimensionless airfoil suction surface velocity distributions that were similar to those of Stage 7. The design process is described in this section.

Design Of Rotor 7/Rotor A

Rotor 7 airfoil sections were designed to be double-circular-arc-type airfoils specified to match the AMAC vector diagram angles shown in dashed lines in Figure 6. The leading edge meanline angles were established by utilizing the Smooth-Flow Incidence Angle Correlation mentioned in Section 5.0. The deviation angles were established by using the CASC procedure described in Section 5.0. The incidence and deviation angles obtained in this manner for Rotor 7 are shown in Figure 14 together with the angles for Rotor A which will be discussed below. The radial variations of Rotor 7 relative air angles and leading and trailing edge metal angles, which are computed from the incidence and deviation angles, are presented in Figure 15. The chordwise variations of meanline angle for the circular-arc meanline of Rotor 7 are shown in Figure 16 for tip, pitch and hub sections. A ΔCAM of -8 degrees was used in the trailing edge region of Rotor 7 in order to retard separation. The need for this ΔCAM will be discussed in more detail in the last paragraph of this section. The airfoil geometry is listed in Table 5. The CASC computer program was used to compute the blade surface velocity distributions for Rotor 7 and the results are shown in Figure 17 for the pitchline and hub sections.

Rotor A airfoil sections were designed to match the vector diagram angles shown in solid lines in Figure 6. The airfoils have modified-circular-arc meanlines, the modifications being necessary to model the dimensionless suction surface velocity distribution of Rotor 7. The iterative design procedure was essentially the same as used for Rotor 7, except that leading edge overcambering (ΔCAM) relative to a circular-arc-type meanline was employed to achieve the modeling described above. Positive ΔCAM increases the leading edge metal angle which makes the incidence angle more negative and also increases suction surface curvature. The combination of these two effects allows suction surface velocities to be modeled over the entire accelerating region. The amount of overcambering required for Rotor A was 6.5 degrees at all radii. The blade surface velocity distributions for Rotor A were computed and the pitchline results are compared with those for Rotor 7 in Figure 17 for the final blade shapes. The two distributions are generally similar, indicating that a satisfactory low speed model has been achieved.

In a recent Low Speed Research Compressor test program, the existence of separated flow on the suction surface of a highly loaded circular-arc rotor hub section, somewhat similar in design to Rotor A, was found experimentally.

A subsequent modification of this rotor hub region by decambering the trailing edge removed the separated flow region at the design point. Since separation was also believed to be likely for the hub region of Rotor A if a circular-arc section were specified, a similar decambering (ΔCAM_{TE} = -8 degrees) was employed in the Rotor A hub region. The effect of decambering the trailing edge hub region is clearly seen in the meanline shown in Figure 16 and in the more linear blade surface velocity distribution shown in Figure 17. A comparison of the design parameters for Rotor 7 and Rotor A is listed in Table 5.

Design Of Stator 7/Stator A

Stator 7 airfoil sections were designed by using a 65-series thickness distribution on a circular arc meanline specified to match the AMAC vector diagram angles shown in dashed lines in Figure 5. The iterative design procedure for Stator 7 was similar to that described for Rotor 7 in Section 5 except that a 65-series thickness distribution was used instead of a double-circular-arc-type distribution. The incidence and deviation angles obtained for Stator 7 are shown in Figure 18. As before, the results for Stator A are also shown in this same figure for comparative purposes and will be discussed later. The radial variation of absolute air angles and leading and trailing edge metal angles is shown in Figure 19. The airfoil geometry is listed in Table 6 and the chordwise variations of meanline angle are shown in Figure 20. The CASC computer program was used to compute the vane surface velocity distributions for Stator 7 and the results are shown in Figure 21 for the pitchline section. The low speed Stage A stator was designed to have a similar distribution.

Stator A airfoil sections were designed to match the vector diagram angles shown in solid lines in Figure 5. These airfoils have a 65-series thickness distribution on a modified circular-arc meanline, the leading edge modification being necessary to model the dimensionless suction surface velocity distribution of Stator 7. The iterative design procedure was the same as used for Stator 7. Stator A required 3.5 degrees of leading edge overcambering (ΔCAM_{LE}) relative to a circular-arc-type meanline in order to model the velocity distribution shown in Figure 21 for Stator 7. Incidence and deviation angles obtained for Stator A are shown in Figure 18 and the radial variations of air angles and metal angles are shown in Figure 19. A comparison of the chordwise variations in meanline angle for Stator A and Stator 7 in Figure 20 shows the amount of overcambering used in the leading edge region. The Stator A airfoil geometry is listed in Table 6.

The CASC computer program was used to compute the vane surface velocity distributions for Stator A. The comparison of Stator A and Stator 7 pitchline velocity distributions is shown in Figure 21 for the final vane shapes. The two distributions are quite similar indicating that a satisfactory low speed model has been achieved.

Design Of The IGV

In order to achieve a repeating stage environment as rapidly as possible, inlet guide vanes are being used to provide the first rotor with the same inlet swirl distribution as shown in Figure 5 for the Stage A stator exit air angle. The IGV was designed following the guidelines of Dunavant (Reference 5). The pitchline solidity of the 53 IGV's was chosen to be approximately 1.0 and the pitchline chord was computed. This chord was held constant and values of solidity across the span were computed. Then values of lift coefficient, C_{L_O}, and angle-of-attack (stagger) were determined from the curves of Dunavant. These values of lift coefficient and angle-of-attack are shown in Figure 22.

7.0 DESIGN OF ROTOR B

Design Concept

Recent low-speed test results from a rotor design somewhat similar to Rotor A indicate that very small rotor wakes are present in the tip region and the large tip loss core is located between wakes. The rotor trailing edge region should, therefore, be able to take higher diffusion rates. Consequently, the Rotor B design concept was to modify the meanline shape in the casing endwall region to unload the leading edge and load the trailing edge region relative to Rotor A. This could reduce tip clearance leakage by reducing the maximum pressure difference across the rotor without undue risk of flow separation. Also, an added efficiency improvement might be expected at higher Mach numbers due to the reduction in peak velocity.

Airfoil Section Shapes

Rotor B was designed to the same inlet and exit air angles as Rotor A using the same design procedures as described in Section 6.0. However, for Rotor B, 2.0 degrees of ΔCAM were specified in the leading edge tip region (Rotor A had 6.5 degrees) and 6.0 degrees of ΔCAM were specified in the trailing edge tip region (Rotor A had 0.0 degrees). In addition, the maximum thickness was moved from 50 percent chord to 60 percent chord, which also gave increased loading in the trailing edge region of Rotor B. This difference between Rotor B and Rotor A in the tip region was gradually reduced in the radial direction so that Rotor B was identical to Rotor A from the pitchline to the hub region. The resulting incidence and deviation angles for Rotor B are compared to those for Rotor A in Figure 23. The radial variation of leading edge and trailing edge metal angle is shown in Figure 24, and comparisons of the chordwise variation of meanline angle for the tip sections of Rotor B and Rotor A are shown in Figure 25. The 4.5 degrees less overcambering in the leading edge region, the 6.0 degrees overcambering in the trailing edge region and the meanline blend points, which specify where the overcambering blends into the circle arc distribution, are evident in Figure 25. The airfoil geometry for Rotor B is listed in Table 7.

The CASC computer program was used to compute the blade surface velocity distributions for Rotor B. The comparison of the Rotor B and Rotor A distributions is shown in Figure 26 for the final blade shapes. The reduced peak suction surface velocity and the increased trailing edge loading for Rotor B are evident in the comparison.

8.0 DESIGN OF STATOR B

Design Concept

Evaluation of existing test data from NASA Contract NAS3-11158 (Reference 6) indicates that rather good performance was achieved from a highly loaded single stage which employed twist gradients in its endwall regions. The apparent success of Stage D of Contract NAS3-11158 suggested that this approach should be tried in the multistage environment. Consequently, the Stator B vanes were twisted closed locally near the endwalls.

Airfoil Section Shapes

Stator B was designed to the inlet and exit absolute air angles shown in solid lines in Figure 9 by using the same design procedures as described in Section 6.0. This design procedure was an iterative technique in which the trailing edge metal angles were obtained as a result of satisfying the Kutta condition in a CASC analysis. An inviscid secondary flow analysis was conducted for Stator B and compared with that for Stator A. Maximum differences were about 1.5 degrees. Slight adjustments were made in X_p to account for those differences.

Stator B was constructed by using a 65-series thickness distribution on a modified circular-arc meanline. Incidence and deviation angles were determined in the same manner as described in Section 6.0 and the results are compared with those for Stator A in Figure 27. The amount of leading edge overcambering required and the airfoil geometry are presented in Table 8. The radial variations of absolute air angles and leading and trailing edge metal angles for Stator B are shown in Figure 28. The comparisons of the meanlines for Stators A and B in Figures 29 and 30 show that the meanline shapes are nearly the same although the curves are displaced from each other due to the twist gradients in the endwall regions of Stator B.

The type of twist employed in Stator B leads to acute angles where the suction surface intersects the endwalls in the leading edge region and obtuse angles near the trailing edge. In order to reduce the acute angles, which are judged to cause increase corner boundary layer growth, the airfoil sections were stacked at 30 percent chord rather than at the usual 50 percent chord location. The change in the stacking axis location and the endwall twist of Stator B have produced a vane shape that is considerably different in appearance from Stator A.

The CASC computer program was used to compute the vane surface velocity distribution for Stator B. The comparison of the Stator B and Stator A distributions is shown in Figures 31 and 32. The shapes of the velocity distributions are virtually identical, with the only difference being in velocity level.

9.0 DESIGN OF STATOR C

Design Concept

Stator C embodies airfoil sections near the endwalls that are similar to the Rotor A hub section in having reduced trailing edge loading. It is believed that this type of airfoil section may reduce flow separation at the junctures of the suction surface and the endwalls.

Airfoil Section Shapes

Stator C was designed to the inlet and exit air angles specified in Figure 5 for Stator A by using the same design procedure described in Section 6.0. Modified circular-arc meanlines were used with 65-series thickness distributions to construct the airfoils. In order to unload the trailing edge region and load the leading edge region of Stator C relative to Stator A, additional overcambering of the meanline was specified in the leading edge region, and decambering was specified in the trailing edge region. Incidence and deviation angles were determined in the same way as described in Section 6.0 and the results are shown in Figure 33. The radial variations of air angles and metal angles are shown in Figure 34 for Stator C. The amount of overcambering specified in the leading edge region and the amount of decambering specified in the trailing edge region are presented in Figures 29 and 30. Airfoil geometry is listed in Table 9.

The CASC computer program was used to compute the vane surface velocity distribution for Stator C. The comparison of the Stator C and Stator A distributions is shown in Figures 31 and 32. Relative to Stator A, the calculated peak suction surface velocity of Stator C has been increased, the loading in the leading edge region has been increased and the loading in the trailing edge region has been decreased. The overall circulation of Stator C is the same as that of Stator A.

10.0 REFERENCES

1. Wisler, D.C., Koch, C.C., Smith, L.H., Jr.; "Preliminary Design Study of Advanced Multistage Axial Flow Core Compressors," NASA CR-135133, February 1977.

2. Koch, C.C., and Smith, L.H., Jr.; "Loss Sources and Magnitudes in Axial-Flow Compressors," Transactions of ASME, Journal of Engineering for Power, Volume 98, Series A, No. 3, July 1976, Page 411.

3. Smith, L.H., Jr.; "Casing Boundary Layers in Multistage Axial-Flow Compressors," Flow Research on Blading, L.S. Dzung, Editor, Elsevier Publishing, Amsterdam, Netherlands, 1970.

4. Prince, D.C., Jr., Wisler, D.C., and Hilvers, D.E.; "Study of Casing Treatment Stall Margin Improvement Phenomena," NASA CR-134552, March 1974.

5. Smith, L.H., Jr.; "The Radial-Equilibrium: Equation of Turbomachinery," Transactions of ASME, Journal of Engineering for Power, Volume 88, Series A, 1966, Page 1.

6. Brent, J.A., and Clemmons, D.R.; "Single-Stage Experimental Evaluation of Tandem-Airfoil Rotor and Stator Blading for Compressors," Final Report NASA CR-134713, November 1974.

7. Dunavant, J.C.; "Cascade Investigation of a Related Series of 6-Percent-Thick-Vane Profiles and Design Charts," NACA TN 3959, May 1957.

Table 1. Design Parameters for AMAC Compressor.

Total Pressure Ratio	23
Number of Stages	10
Corrected Inlet Tip Speed, m/sec (fps)	469 (1540)
Physical Inlet Tip Speed, m/sec (fps)	485 (1590)
Physical Rear Hub Speed, m/sec (fps)	370 (1214)
Physical Speed, rpm	13,900
Inlet Radius Ratio	0.496
Inlet Specific Flow, kg/sec-m^2 (lb/sec-ft^2)	178 (36.5)
Inlet Corrected Flow, (lb_m/sec)	103.3
Inlet Tip Diameter, m (in.)	0.6660 (26.22)
Exit Radius Ratio	0.930
Exit Mach Number	0.26
Exit Tip Diameter, m (in.)	0.5456 (21.48)
Length to OGV Exit, m (in.)	0.6614 (26.04)
Length to Diffuser Exit, m (in.)	0.6900 (27.16)
Number of Airfoils	1959
Average Aspect Ratio	1.72
Average Solidity	1.40
Average Swirl, Degree	20.4
Average Reaction	0.695
Stall Margin, %	18
Adiabatic Efficiency at OGV Exit	0.860
Adiabatic Efficiency at Diffuser Exit	0.853
Compressor Weight, kg (lb)	269 (592)

Table 2. Design Parameters for AMAC Stage 7 and the Low Speed Stage A.

Design Parameter	AMAC Stage 7	Stage A Low Speed Model
Flow Coefficient	0.442	0.442†
Pressure-Rise Coefficient	0.638	0.647‡
Reaction Ratio	0.682	0.628
Rotor Inlet Hub:Tip Radius Ratio	0.893	0.850
Tip Diameter cm (in.)	56.64 (22.3)	152.4 (60.0)
Rotor Tip Clearance/Blade Height, %	1.28	1.35
Average Reynolds Number Based on U_{Tip}	740,000	360,000
Rotor Pitch Inlet Rel. Air Angle, deg	59.7	60.1
Rotor Pitch Exit Rel. Air Angle, deg	45.6	44.1
Rotor Pitch Inlet Mach Number	0.74	0.146
Rotor Axial Velocity Ratio	0.93	1.00
Rotor Pitch Diffusion Factor	0.481	0.470
Rotor Aspect Ratio	1.28	1.20
Rotor Pitch Solidity	1.25	1.16
Stator Pitch Inlet Abs. Air Angle, deg	49.7	50.5
Stator Pitch Exit Abs. Air Angle, deg.	21.0	21.0
Stator Pitch Inlet Mach Number	0.55	0.112
Stator Axial Velocity Ratio	0.998	1.00
Stator Pitch Diffusion Factor	0.465	0.464
Stator Aspect Ratio	1.37	1.21
Stator Pitch Solidity	1.67	1.58

† The flow coefficient was computed as the average rotor inlet axial velocity divided by the rotor pitch speed, using the full physical annulus area (blockage = 1.0). Based on the rotor tip speed, this flow coefficient becomes 0.407.

‡ The pressure coefficient was computed by using the rotor pitchline wheel speed. Based on rotor tip speed, this value becomes 0.555. Normalization of experimental data will be done using rotor tip speed, consistent with past General Electric practice for Low Speed Research Compressor data.

Table 3. Vector Diagram Parameters for AMAC Stage 7 and Stage A.

	Tip						Pitch						Hub	
Rotor Inlet	SL1† Stg.7	SL1 Stg. A	SL2 Stg.A	SL3 Stg.A	SL4 Stg.A	SL5 Stg.A	SL6 Stg.7	SL6 Stg.A	SL7 Stg.A	SL8 Stg.A	SL9 Stg.A	SL10 Stg.A	SL11 Stg.7	SL11 Stg.A
r (cm)	-	76.20	75.02	73.88	72.76	71.65	-	70.55	69.44	68.32	67.17	66.0	-	64.77
U (m/sec)	399.0	57.61	56.71	55.85	55.00	54.17	377.6	53.33	52.50	51.65	50.78	49.98	355.8	48.97
V'_θ (m/sec)	320.9	46.98	46.64	46.06	42.25	44.30	307.8	43.49	42.48	41.50	40.50	39.29	276.9	38.04
V_Z (m/sec)	159.7	21.78	23.01	24.03	24.76	25.27	182.6	25.62	25.83	25.92	25.75	25.30	177.1	24.54
β' (deg)	63.4	65.1	63.7	62.4	61.3	60.3	59.3	59.5	58.7	58.0	57.6	57.2	57.4	57.2
M'	.740	.152	.153	.153	.151	.150	.757	.148	.146	.144	.141	.137	.684	.133
Rotor Exit														
r (cm)	-	76.20	74.97	73.82	72.71	71.62	-	70.52	69.42	68.30	67.16	65.99	-	64.77
U (m/sec)	397.3	57.61	56.68	55.81	54.97	54.14	376.7	53.32	52.48	51.63	50.77	49.89	356.1	48.97
V'_θ (m/sec)	179.3	28.01	28.18	27.99	27.34	26.34	172.4	25.18	23.77	22.28	29.52	18.68	126.6	16.46
V_Z (m/sec)	134.5	20.18	22.56	24.07	24.92	25.41	178.2	25.71	25.79	25.84	25.74	25.32	165.0	24.72
β' (deg)	53.0	54.2	51.3	49.3	47.6	46.0	46.2	44.4	42.7	40.8	38.7	36.4	37.5	33.7
M'	.450	.101	.106	.108	.108	.107	.514	.106	.103	.100	.097	.092	.423	.087
Stator Inlet														
r (cm)	-	76.20	74.97	73.82	72.71	71.62	-	70.52	69.42	68.30	67.16	65.99	-	64.77
V_θ (m/sec)	218.5	29.59	28.50	27.82	27.63	27.80	197.2	28.14	28.71	29.35	30.13	31.21	229.2	32.51
V_Z (m/sec)	137.6	20.18	22.56	24.07	24.92	25.41	178.2	25.71	25.79	25.84	25.74	25.32	170.7	24.72
β (deg)	57.4	55.7	51.6	49.1	48.0	47.6	47.9	47.6	48.1	48.6	49.5	51.0	53.3	52.8
M	.520	.105	.107	.108	.109	.110	.549	.112	.113	.115	.116	.118	.581	.120
Stator Exit														
r (cm)	-	76.20	75.02	73.88	72.76	71.65	-	70.55	69.44	68.32	67.17	66.00	-	64.77
V_θ (m/sec)	78.0	10.55	10.01	9.72	9.68	9.73	69.4	9.77	9.94	10.07	10.20	10.51	77.8	10.84
V_Z (m/sec)	153.9	21.63	22.85	23.84	24.57	25.08	174.3	25.43	25.64	25.73	25.56	25.09	167.6	24.36
β (deg)	26.8	26.0	23.6	22.2	21.5	21.2	21.7	21.0	21.2	21.4	21.8	22.7	24.9	24.0
M	.343	.070	.073	.075	.077	.079	.382	.080	.081	.081	.081	.080	.369	.078

† SL ≡ Streamline

ORIGINAL PAGE IS
OF POOR QUALITY

Table 4. Vector Diagram Parameters for Stator B.

	Tip SL1† Stg.B	SL2 Stg.B	SL3 Stg.B	SL4 Stg.B	SL5 Stg.B	Pitch SL6 Stg.B	SL7 Stg.B	SL8 Stg.B	SL9 Stg.B	SL10 Stg.B	Hub SL11 Stg.B
Rotor Inlet											
r (cm)	76.20	74.96	73.80	72.70	71.62	70.54	69.45	68.36	67.23	66.05	64.77
U (m/sec)	57.61	56.66	55.81	54.96	54.13	53.31	52.52	51.66	50.81	49.93	48.95
V'_θ (m/sec)	44.10	45.45	46.06	45.96	45.42	44.56	43.65	42.49	40.90	38.59	34.99
V_Z (m/sec)	20.03	22.34	24.17	25.24	25.91	26.27	26.49	26.46	25.97	24.96	22.89
β' (deg)	65.6	63.7	62.3	61.2	60.3	59.5	58.8	58.1	57.6	57.1	56.8
M'	.142	.149	.152	.154	.153	.152	.150	.147	.142	.135	.122
Rotor Exit											
r (cm)	76.20	74.81	73.66	72.58	71.53	70.49	69.44	68.37	67.27	66.11	64.77
U (m/sec)	57.61	56.57	55.69	54.86	54.07	53.28	52.49	51.69	50.87	49.99	48.95
V'_θ (m/sec)	25.39	26.94	27.83	27.92	27.28	26.18	24.90	23.32	21.12	18.14	13.56
V_Z (m/sec)	16.40	21.76	24.60	26.09	26.79	27.04	27.13	27.04	26.37	24.81	21.00
β' (deg)	57.1	51.1	48.5	47.0	45.5	44.1	42.5	40.7	38.7	36.1	32.9
M'	.088	.101	.109	.112	.112	.110	.108	.104	.099	.090	.073
Stator Inlet											
r (cm)	76.20	74.81	73.65	72.57	71.53	70.49	69.44	68.37	67.27	66.11	64.77
V_θ (m/sec)	32.22	29.63	27.86	26.94	26.79	27.10	27.58	28.38	29.75	31.85	35.39
V_Z (m/sec)	16.40	21.73	24.60	26.09	26.79	27.04	27.16	27.04	26.37	24.81	21.00
β (deg)	63.0	53.7	48.6	45.9	45.0	45.1	45.5	46.4	48.5	52.1	59.3
M	.106	.107	.109	.110	.111	.112	.113	.115	.116	.118	.120
Stator Exit											
r (cm)	76.20	74.96	73.81	72.71	71.63	70.55	69.46	68.36	67.23	66.05	64.77
V_θ (m/sec)	13.41	11.16	9.69	8.93	8.66	8.66	8.78	9.08	9.85	11.22	13.87
V_Z (m/sec)	19.90	22.34	23.99	25.5	25.69	26.06	26.27	26.24	25.79	24.75	22.71
β (deg)	34.0	26.5	22.0	19.6	18.6	18.4	18.5	19.1	20.9	24.4	31.4
M	.070	.073	.076	.078	.079	.080	.081	.081	.081	.079	.078

† SL ≡ Streamline

Table 5. Rotor 7 and Rotor A Airfoil Geometry.

	Tip						Pitch						Hub	
	SL1† R7	SL1 RA	SL2 RA	SL3 RA	SL4 RA	SL5 RA	SL6 R7	SL6 RA	SL7 RA	SL8 RA	SL9 RA	SL10 RA	SL11 R7	SL11 RA
Avg. Radius, r (cm)	-	76.200	75.057	73.914	72.771	71.628	-	70.485	69.342	68.199	67.056	65.913	-	64.770
Chord, c (cm)	-	9.550	9.550	9.550	9.550	9.550	-	9.550	9.550	9.550	9.550	9.550	-	9.550
Solidity, σ	1.183	1.076	1.093	1.110	1.127	1.145	1.250	1.163	1.182	1.202	1.223	1.244	1.323	1.265
β_1*	65.19	74.00	72.80	71.50	70.30	69.25	60.80	68.40	67.70	67.20	67.30	67.80	59.35	68.50
β_2*	44.23	43.40	43.20	42.10	40.40	38.50	40.20	36.60	34.9	33.20	31.60	30.00	30.00	28.40
Incidence, i (deg)	-1.69	-8.87	-9.05	-9.06	-8.99	-8.92	-1.50	-8.90	-9.01	-9.18	-9.74	-10.58	-1.95	-11.32
Deviation, δ (deg)	8.97	10.83	8.12	7.20	7.25	7.53	6.00	7.80	7.77	7.57	7.12	6.40	7.50	5.26
Camber, ϕ (deg)	20.96	30.6	29.6	29.4	29.9	30.75	20.68	31.8	32.8	34.0	35.7	37.8	29.34	40.1
Stagger, ξ (deg)	54.71	56.53	55.83	54.64	53.20	51.73	50.49	50.36	49.18	47.87	46.5	44.86	44.68	42.91
ΔCAM_{LE} (deg)	0	6.50	6.50	6.50	6.50	6.50	0	6.50	6.50	6.60	7.10	7.72	2.00	8.50
ΔCAM_{TE} (deg)	0	0	0	0	0	0	0	0	0	-0.50	-1.90	-4.35	-8.00	-8.00
$Blend_{LE}$, %c	-	40	40	40	40	40	-	40	40	40	40	40	-	40
$Blend_{TE}$, %c	-	-	-	-	-	-	-	-	-	60	60	60	-	60
t_{max}/c	0.043	0.043	0.046	0.050	0.054	0.058	0.062	0.062	0.066	0.070	0.074	0.080	0.085	0.085
t_{TE}/c	0.011	0.011	0.011	0.012	0.012	0.013	0.013	0.013	0.013	0.014	0.014	0.015	0.015	0.015
t_{max} Location, %c	50	50	50	50	50	50	50	50	50	49	46	43	50	40

† SL ≡ Streamline

ORIGINAL PAGE IS
OF POOR QUALITY

Table 6. Stator 7 and Stator A Airfoil Geometry.

	OD S7	OD SA	SL2 † SA	SL3 SA	SL4 SA	SL5 SA	Pitch S7	Pitch SA	SL7 SA	SL8 SA	SL9 SA	SL10 SA	ID S7	ID SA
Avg. Radius, r (cm	-	76.200	75.057	73.914	72.771	71.628	-	70.485	69.342	68.199	67.056	65.913	-	67.770
Chord, c (cm)	-	9.055	8.923	8.799	8.700	8.606	-	8.534	8.484	8.446	8.420	8.395	-	8.382
Solidity, σ	1.477	1.400	1.400	1.402	1.408	1.415	1.400	1.426	1.441	1.458	1.479	1.500	1.400	1.524
β_1* (deg)	60.85	61.37	57.60	54.95	53.60	53.40	51.30	53.45	53.95	54.80	55.90	57.40	56.90	59.20
β_2* (deg)	12.95	11.00	12.50	13.45	14.00	14.24	15.50	14.40	14.38	14.31	14.22	14.10	16.60	14.00
Incidence, i (deg)	-3.45	-5.67	-5.96	-5.82	-5.65	-5.83	-3.40	-5.86	-5.88	-6.16	-6.40	-6.45	-3.60	-6.45
Deviation, δ (deg)	13.85	15.00	11.15	8.73	7.50	6.69	6.20	6.16	6.80	7.07	7.54	8.63	8.30	10.0
Camber, ϕ (deg)	47.9	50.37	45.10	41.50	39.60	39.16	35.79	39.05	39.57	40.49	41.68	43.30	40.3	45.20
Stagger, ξ (deg)	36.75	35.00	33.85	32.98	32.58	32.60	33.40	32.70	32.94	33.34	33.84	34.54	36.90	35.40
ΔCAM_{LE}, (deg)	0	3.50	3.50	3.50	3.50	3.50	0	3.50	3.50	3.50	3.50	3.50	0	3.50
ΔCAM_{TE}, (deg)	0	0	0	0	0	0	0	0	0	0	0	0	0	0
$Blend_{LE}$, %c	-	40	40	40	40	40	-	40	40	40	40	40	-	40
t_{max}/c	0.090	0.090	0.084	0.084	0.081	0.078	0.075	0.075	0.072	0.069	0.066	0.063	0.060	0.060
t_{TE}/c	0.018	0.018	0.017	0.017	0.016	0.016	0.015	0.015	0.014	0.014	0.013	0.013	0.012	0.012
t_{max} Location, %c	42	42	42	42	42	42	42	42	42	42	42	42	42	42

† SL ≡ Streamline

Table 7. Rotor B Airfoil Geometry.

	Tip SL1†	SL2	SL3	SL4	SL5	Pitch SL6	SL7	SL8	SL9	SL10	Hub SL11
Avg. Radius, r (cm)	76.200	75.057	73.914	72.771	71.628	70.485	69.342	68.199	67.056	65.913	67.770
Chord, c (cm)	9.550	9.550	9.550	9.550	9.550	9.550	9.550	9.550	9.550	9.550	9.550
Solidity, σ	1.076	1.093	1.110	1.127	1.145	1.163	1.182	1.202	1.222	1.243	1.265
β_1* (deg)	70.7	70.67	70.51	69.89	69.13	68.40	67.70	67.20	67.30	67.80	68.50
β_2* (deg)	40.00	40.47	40.36	39.40	38.08	36.60	34.9	33.20	31.60	30.00	28.40
Incidence, i (deg)	-5.57	-6.92	-8.07	-8.58	-8.80	-8.90	-9.01	-9.18	-9.74	-10.58	-11.32
Deviation, δ (deg)	14.23	10.85	8.94	8.25	7.95	7.80	7.77	7.57	7.12	6.40	5.26
Camber, ϕ (deg)	30.70	30.26	30.20	30.15	30.49	31.05	31.80	32.80	34.00	37.80	40.10
Stagger, ξ (deg)	56.93	56.26	56.10	54.98	53.30	51.66	50.36	49.18	47.87	44.86	42.90
ΔCAM_{LE}, (deg)	2.00	3.30	4.50	5.64	6.30	6.50	6.50	6.60	7.10	7.72	8.50
ΔCAM_{TE}, (deg)	6.00	4.35	2.78	1.40	0.35	0	0	-0.5	-1.90	-4.35	-8.00
$Blend_{LE}$, %c	40	40	40	40	40	40	40	40	40	40	40
$Blend_{TE}$, %c	60	60	60	60	60	-	-	60	60	60	60
t_{max}/c	0.043	0.046	0.050	0.054	0.058	0.062	0.066	0.070	0.075	0.080	0.085
t_{TE}/c	0.011	0.011	0.012	0.012	0.013	0.013	0.013	0.014	0.014	0.015	0.015
t_{max} Location, %c	60	57	54	52	51	50	50	49	46	43	40

† SL ≡ Streamline

ORIGINAL PAGE IS
OF POOR QUALITY

Table 8. Stator B Airfoil Geometry.

	OD SL1 †	SL2	SL3	SL4	SL5	Pitch SL6	SL7	SL8	SL9	SL10	ID SL11
Avg. Radius, r (cm)	76.200	75.057	73.914	72.771	71.628	70.485	69.342	68.199	67.056	65.913	64.770
Chord, c (cm)	9.055	8.923	8.799	8.692	8.606	8.534	8.484	8.446	8.415	8.395	8.382
Solidity, σ	1.400	1.400	1.402	1.407	1.415	1.426	1.440	1.458	1.480	1.500	1.524
β_1* (deg)	69.40	61.20	55.50	52.90	52.00	52.00	52.60	53.80	55.90	59.60	65.80
β_2* (deg)	20.80	15.00	12.50	11.70	11.50	11.50	11.70	12.20	13.30	15.60	22.00
Incidence, i (deg)	-6.40	-7.50	-6.90	-7.00	-7.00	-6.90	-7.10	-7.00	-7.40	-7.50	-6.50
Deviation, δ (deg)	13.20	11.50	9.50	7.90	7.10	6.90	6.80	6.90	7.60	8.80	9.40
Camber, ϕ (deg)	45.10	42.70	39.50	37.70	37.00	37.00	37.40	38.10	39.10	40.50	40.30
Stagger ξ (deg)	43.35	36.35	32.25	30.55	30.00	30.00	30.40	31.25	32.85	35.85	42.15
ΔCAM_{LE}	3.50	3.50	3.50	3.50	3.50	3.50	3.50	3.50	3.50	3.50	3.50
ΔCAM_{TE}	0	0	0	0	0	0	0	0	0	0	0
$Blend_{LE}$, %c	40	40	40	40	40	40	40	40	40	40	40
t_{max}/c	0.90	0.087	0.084	0.081	0.078	0.075	0.072	0.069	0.066	0.063	0.060
t_{TE}/c	0.022	0.019	0.017	0.016	0.016	0.015	0.014	0.014	0.013	0.014	0.015
t_{max} Location, %c	42	42	42	42	42	42	42	42	42	42	42

† SL ≡ Streamline

Table 9. Stator C Airfoil Geometry.

	OD SL1†	SL2	SL3	SL4	SL5	Pitch SL6	SL7	SL8	SL9	SL10	ID SL11
Avg. Radius, r (cm)	76.200	75.057	73.914	72.771	71.628	70.485	69.342	68.199	67.056	65.913	67.770
Chord, c (cm)	9.055	8.923	3.799	8.700	8.606	8.534	8.484	8.446	8.420	8.395	8.382
Solidity, σ	1.400	1.400	1.402	1.408	1.415	1.426	1.441	1.458	1.479	1.500	1.524
β_1* (deg)	65.20	60.20	54.50	54.20	53.40	53.45	53.95	55.20	57.20	59.80	63.20
β_2* (deg)	17.00	15.50	14.50	14.25	14.24	14.40	14.75	15.40	16.50	18.00	19.80
Incidence, i (deg)	-9.50	-8.56	-7.37	-6.25	-5.83	-5.86	-5.88	-6.56	-7.70	-8.85	-10.45
Deviation, δ (deg)	9.00	8.15	7.68	7.25	6.96	6.61	6.43	5.98	5.26	4.73	4.20
Camber, ϕ (deg)	69.20	57.40	47.40	39.25	35.66	35.55	35.70	39.10	46.10	54.50	64.40
Stagger, ξ (deg)	26.60	27.70	29.20	31.08	32.07	32.18	32.60	32.15	30.55	28.75	27.00
ΔCAM_{LE} (deg)	4.00	3.80	3.60	3.50	3.50	3.50	3.50	3.50	3.60	3.80	4.00
ΔCAM_{TE} (deg)	-25.00	-16.50	-9.00	-2.80	0	0	0	-2.80	-9.00	-16.50	-25.00
$Blend_{LE}$, %c	20	28	34	37	40	40	40	37	34	28	20
$Blend_{TE}$, %c	35	37	39	40	-	-	-	40	39	37	35
t_{max}/c	0.090	0.081	0.084	0.081	0.078	0.075	0.072	0.069	0.066	0.063	0.060
t_{TE}/c	0.018	0.017	0.017	0.016	0.016	0.015	0.014	0.014	0.013	0.013	0.012
t_{max} Location, %c	42	42	42	42	42	42	42	42	42	42	42

† SL ≡ Streamline

ORIGINAL PAGE IS
OF POOR QUALITY

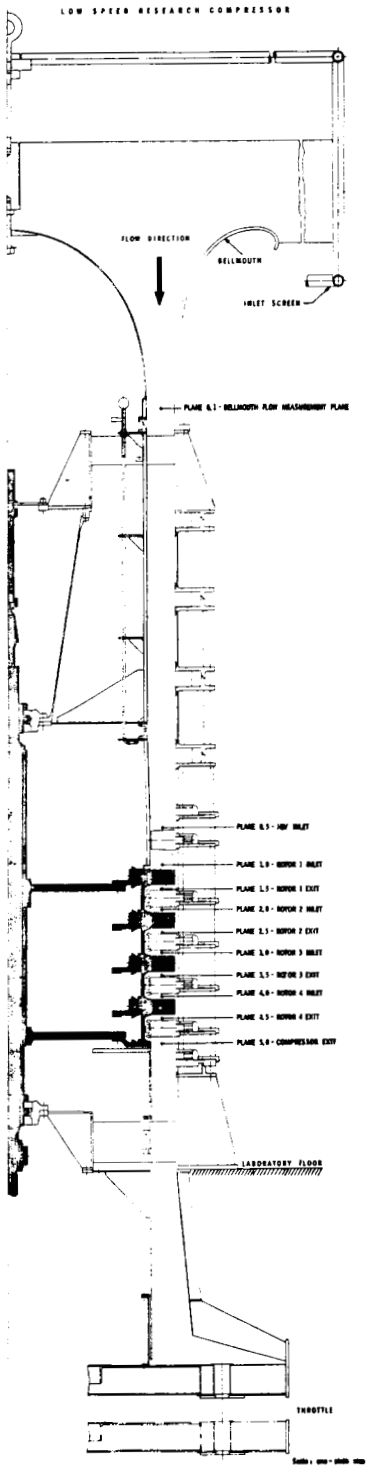

Figure 1. Four Stage Compressor Configuration to be Tested in the NASA/GE Core Compressor Exit Stage Study.

ORIGINAL PAGE IS
OF POOR QUALITY

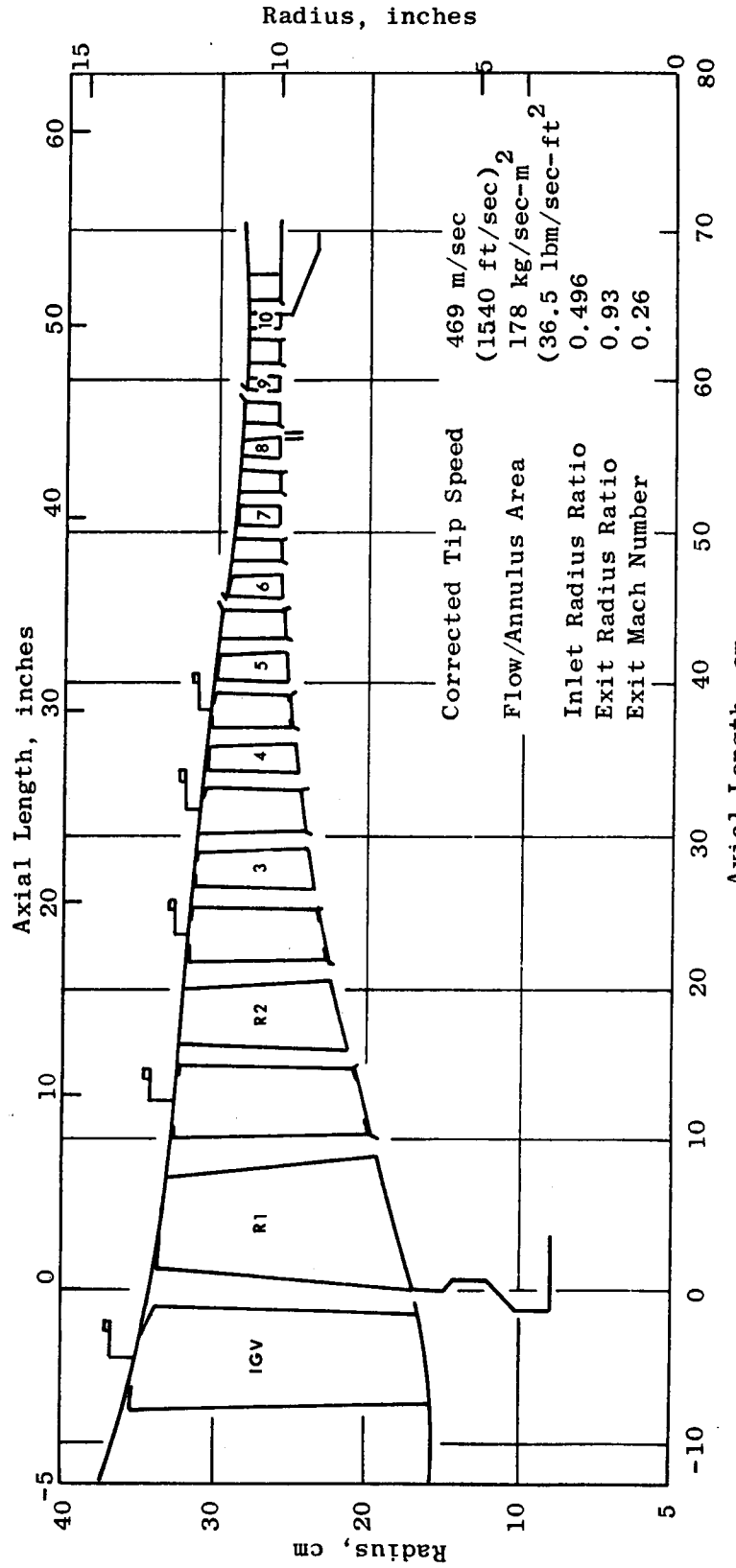

Figure 2. Flowpath of Recommended AMAC Compressor.

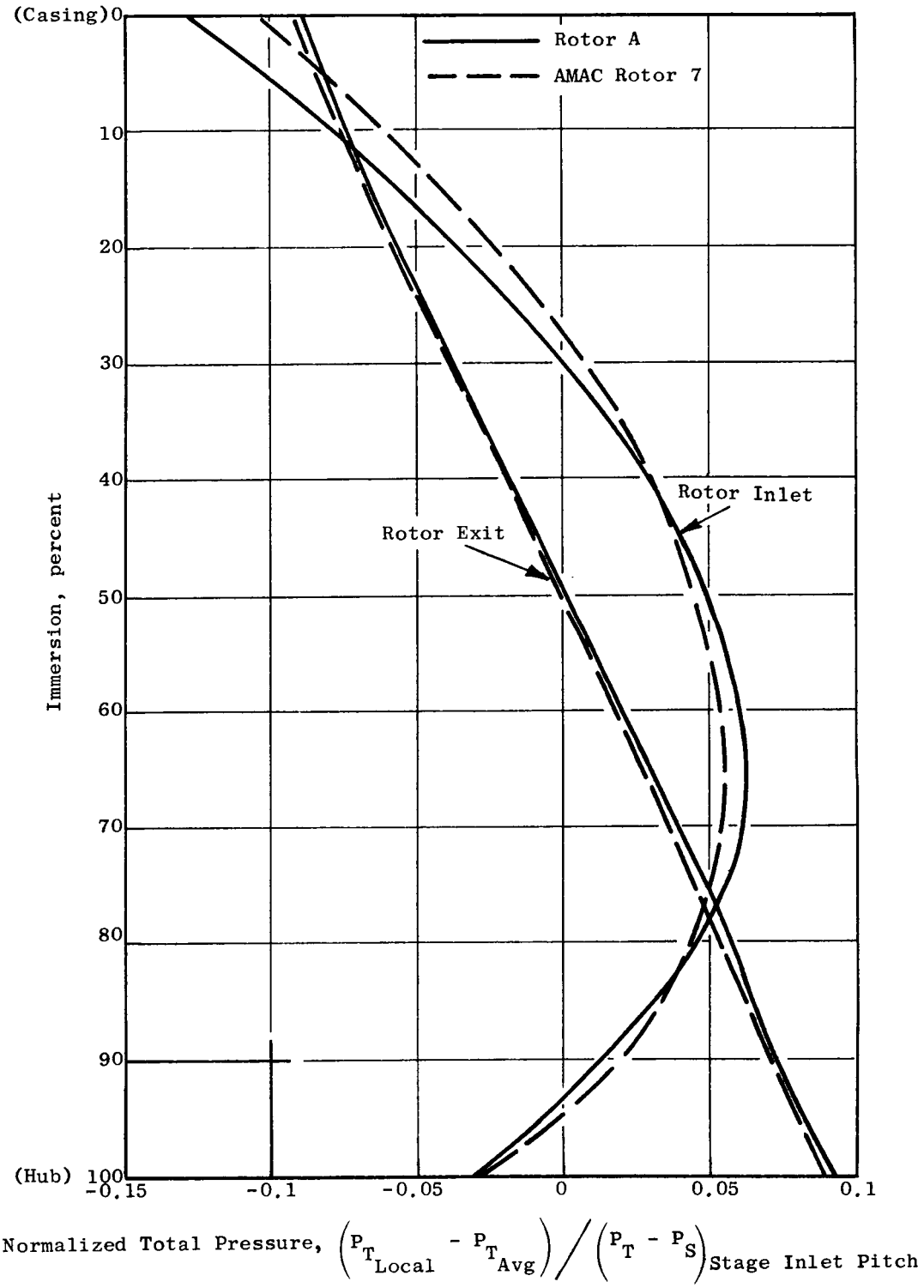

Figure 3. Radial Variation of Normalized Inlet and Exit Total Pressure for AMAC Rotor 7 and the Low Speed Model Rotor A.

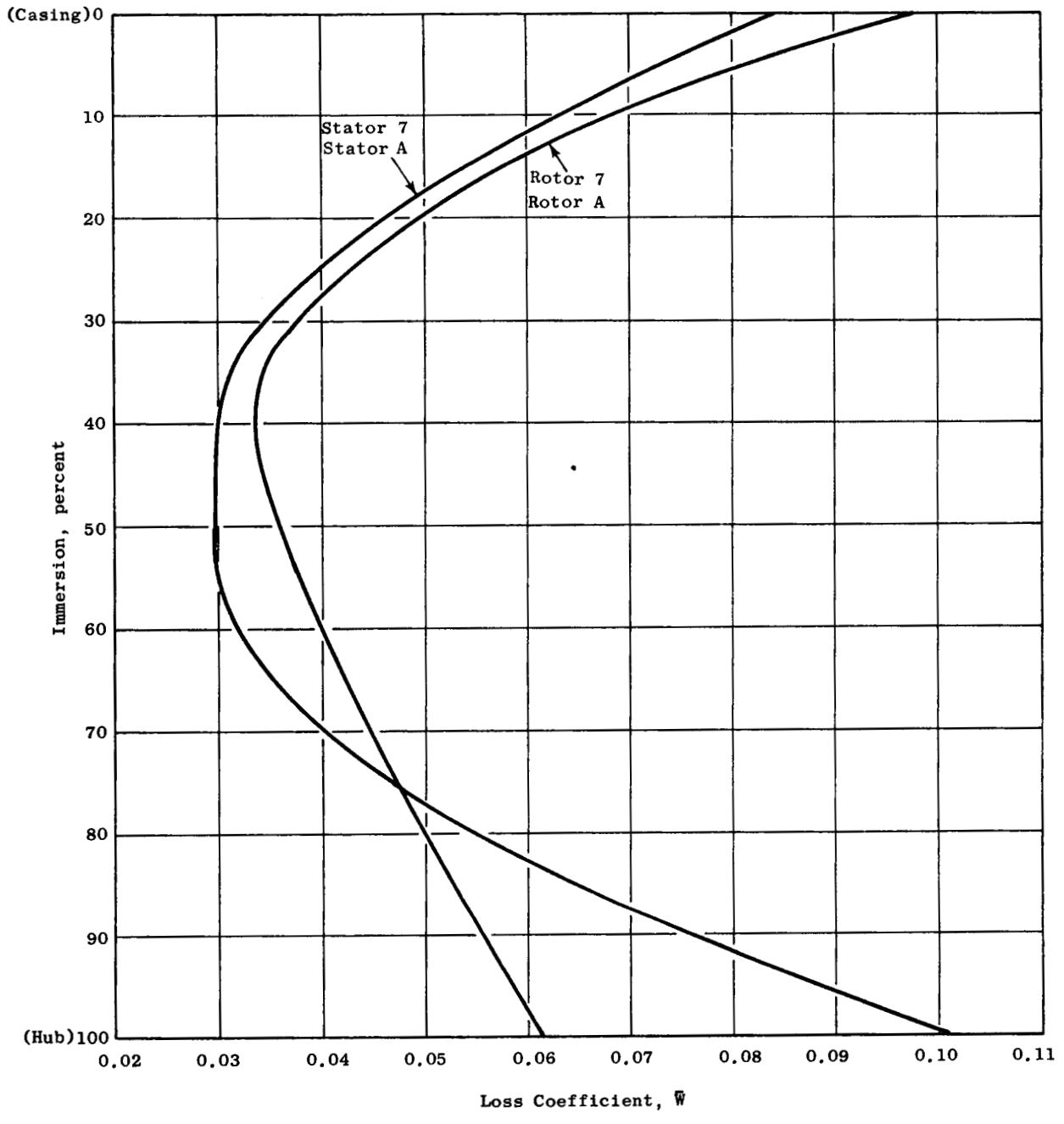

Figure 4. Rotor and Stator Loss Coefficients Versus Percent Immersion for AMAC Stage 7 and the Low Speed Stage A.

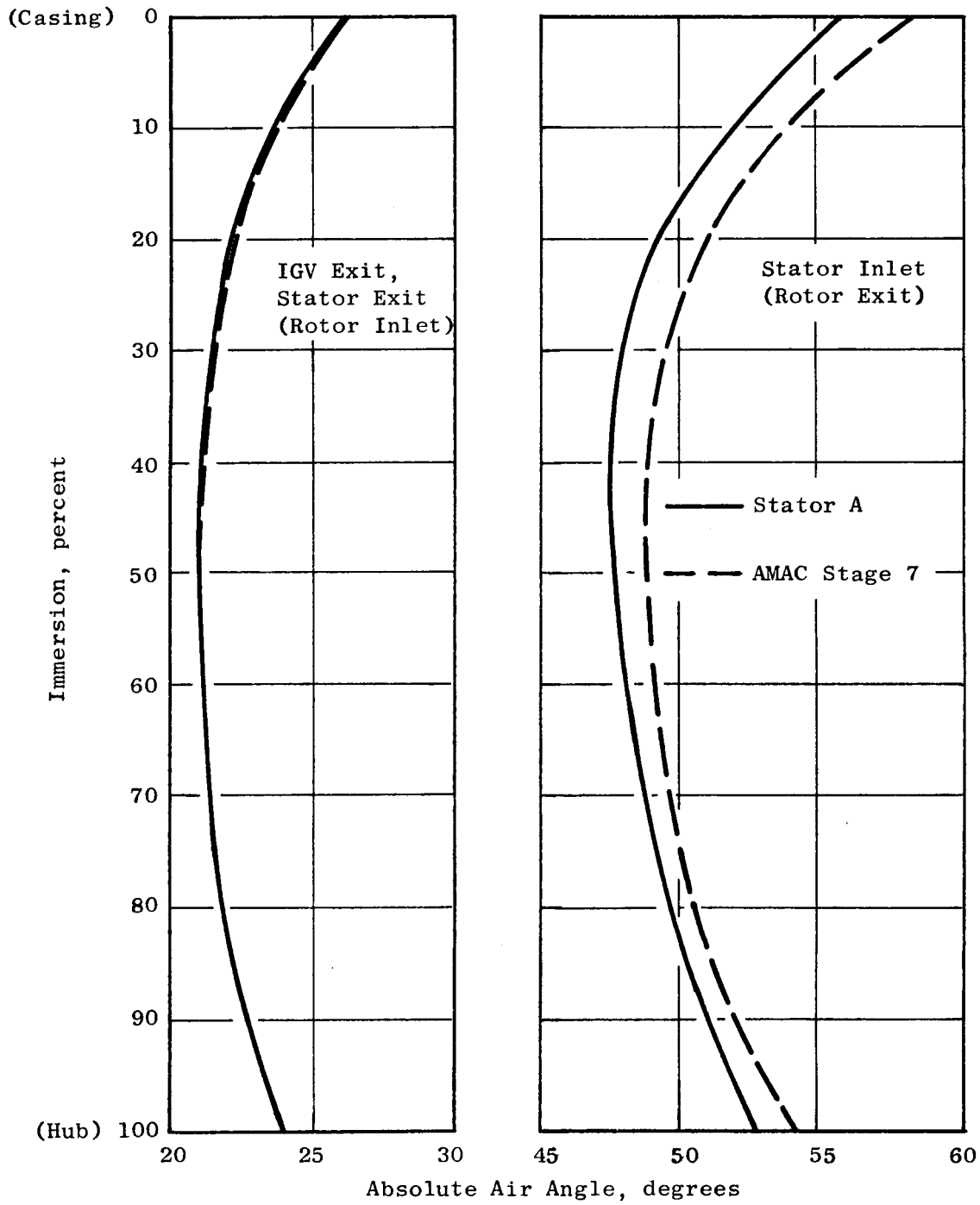

Figure 5. Comparison of the Radial Variation of Stator Absolute Air Angles for Stage 7 of the AMAC Compressor and for the Low Speed Model Stage A.

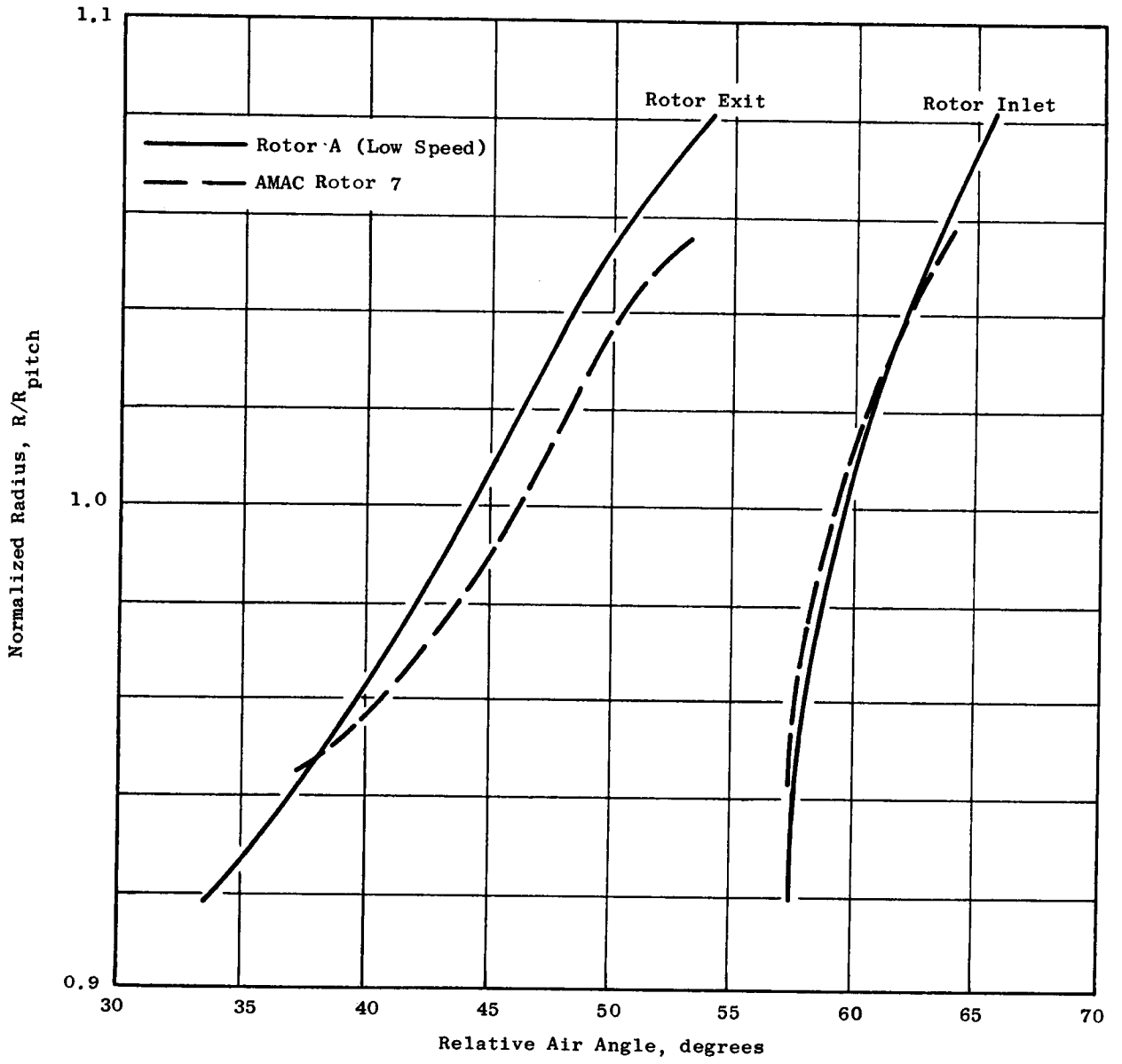

Figure 6. Comparison of the Radial Variation of Rotor Relative Air Angles for Stage 7 of the AMAC Compressor and for the Low Speed Model Stage A.

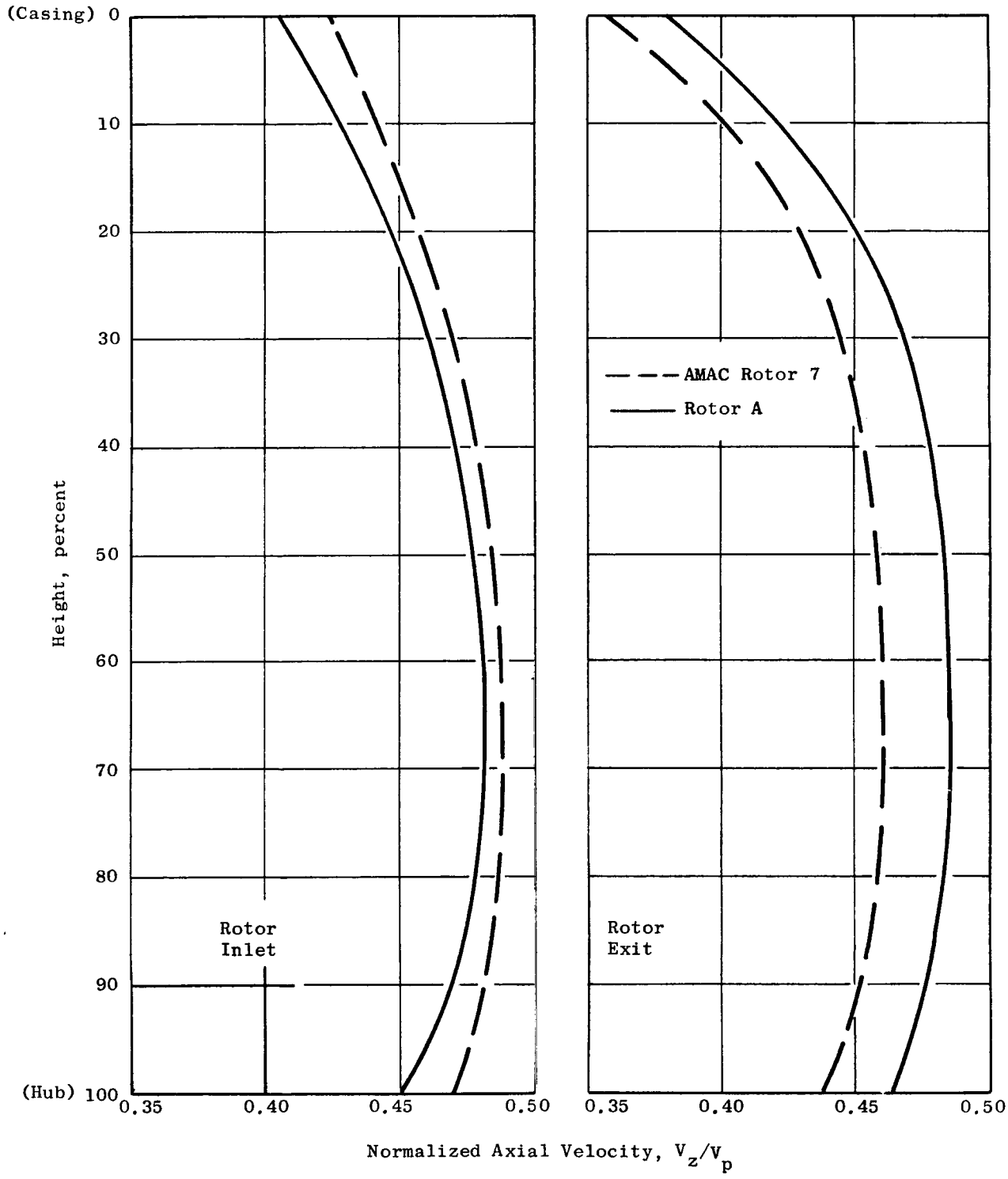

Figure 7. Rotor Inlet and Exit Normalized Axial Velocity Versus Percent Height for AMAC Rotor 7 and Rotor A.

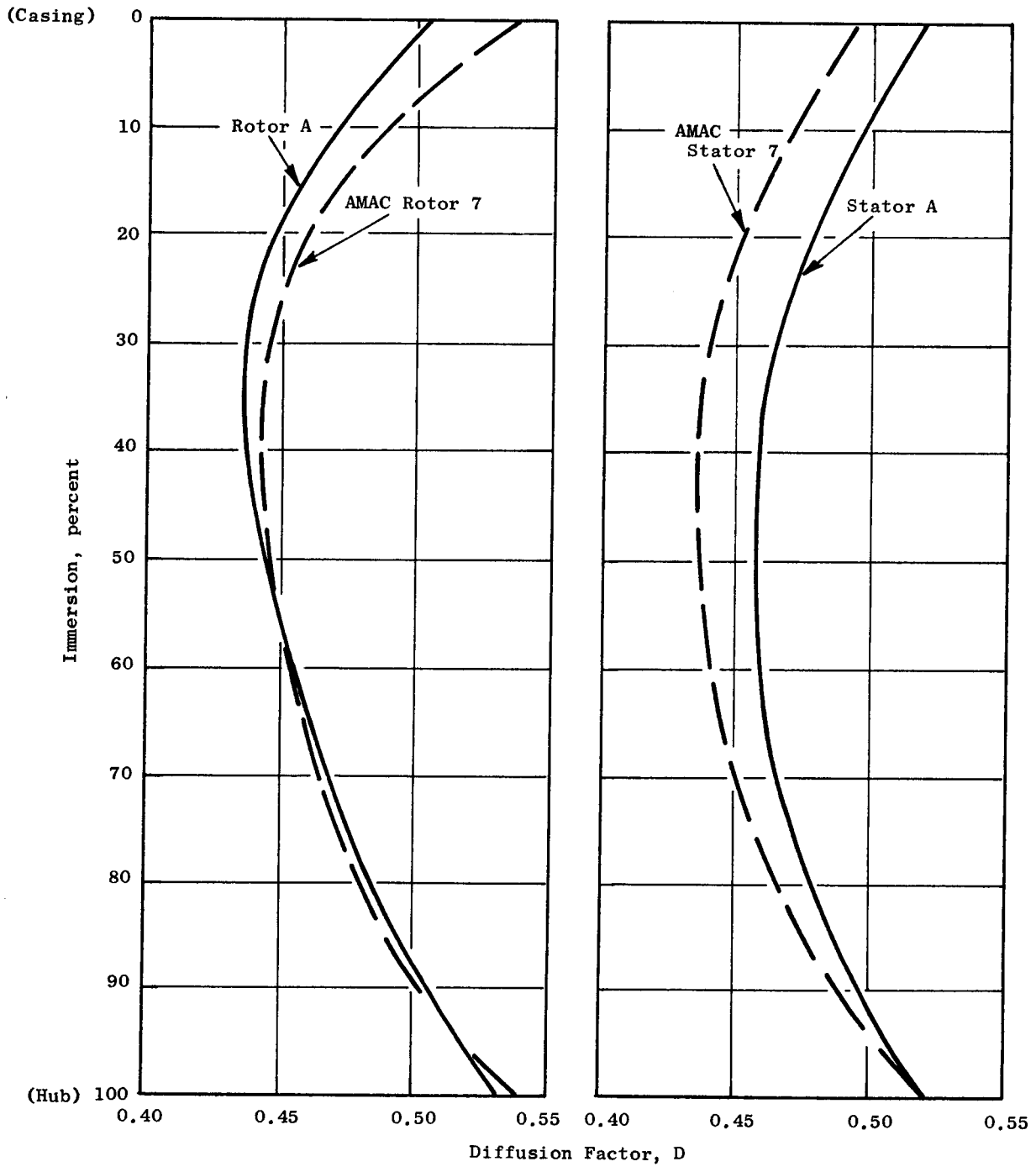

Figure 8. Rotor and Stator Diffusion Factors Versus Percent Immersion for AMAC Stage 7 and Stage A.

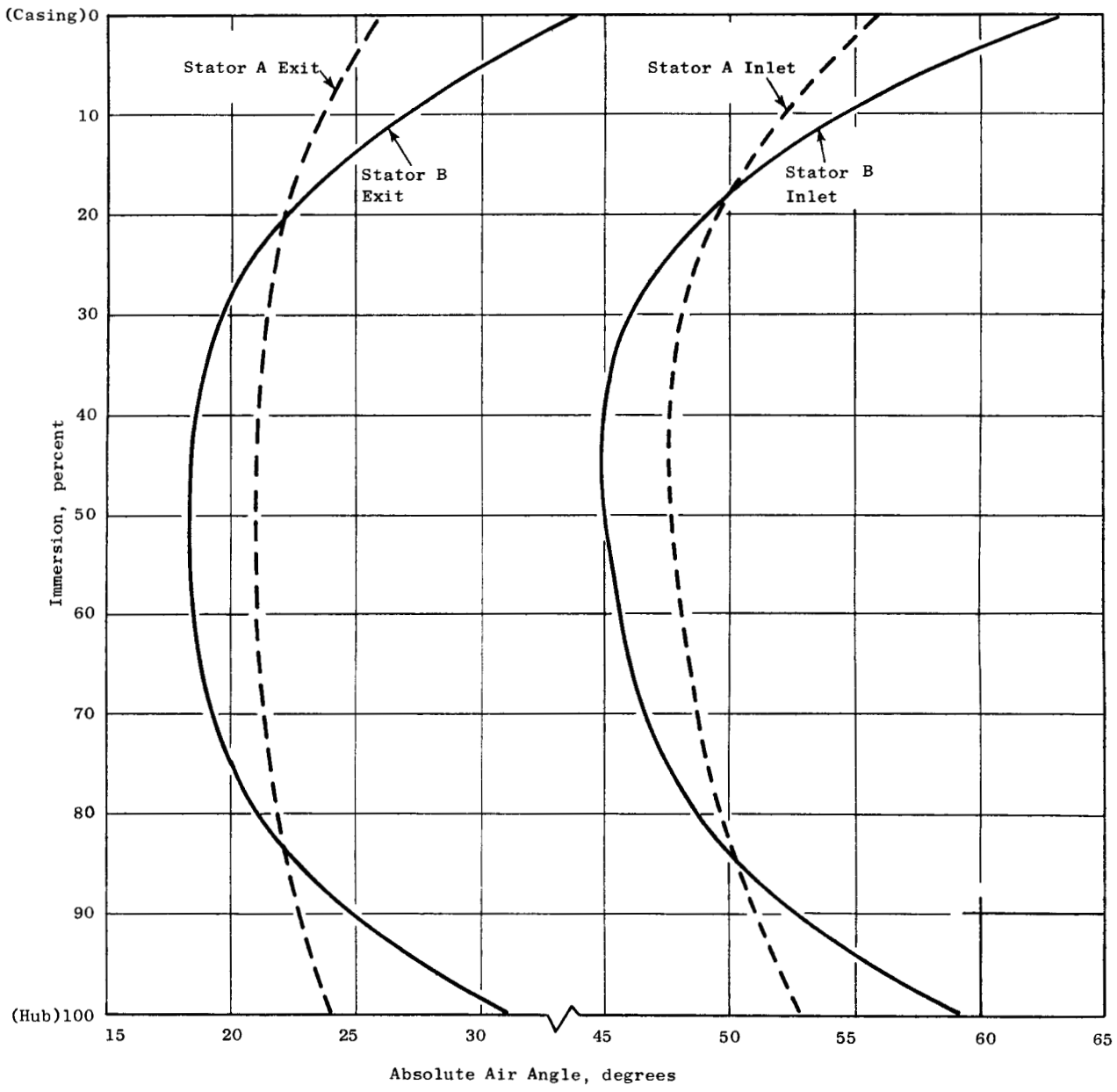

Figure 9. Comparison of the Radial Variation of Inlet and Exit Absolute Air Angle for Stator A and Stator B.

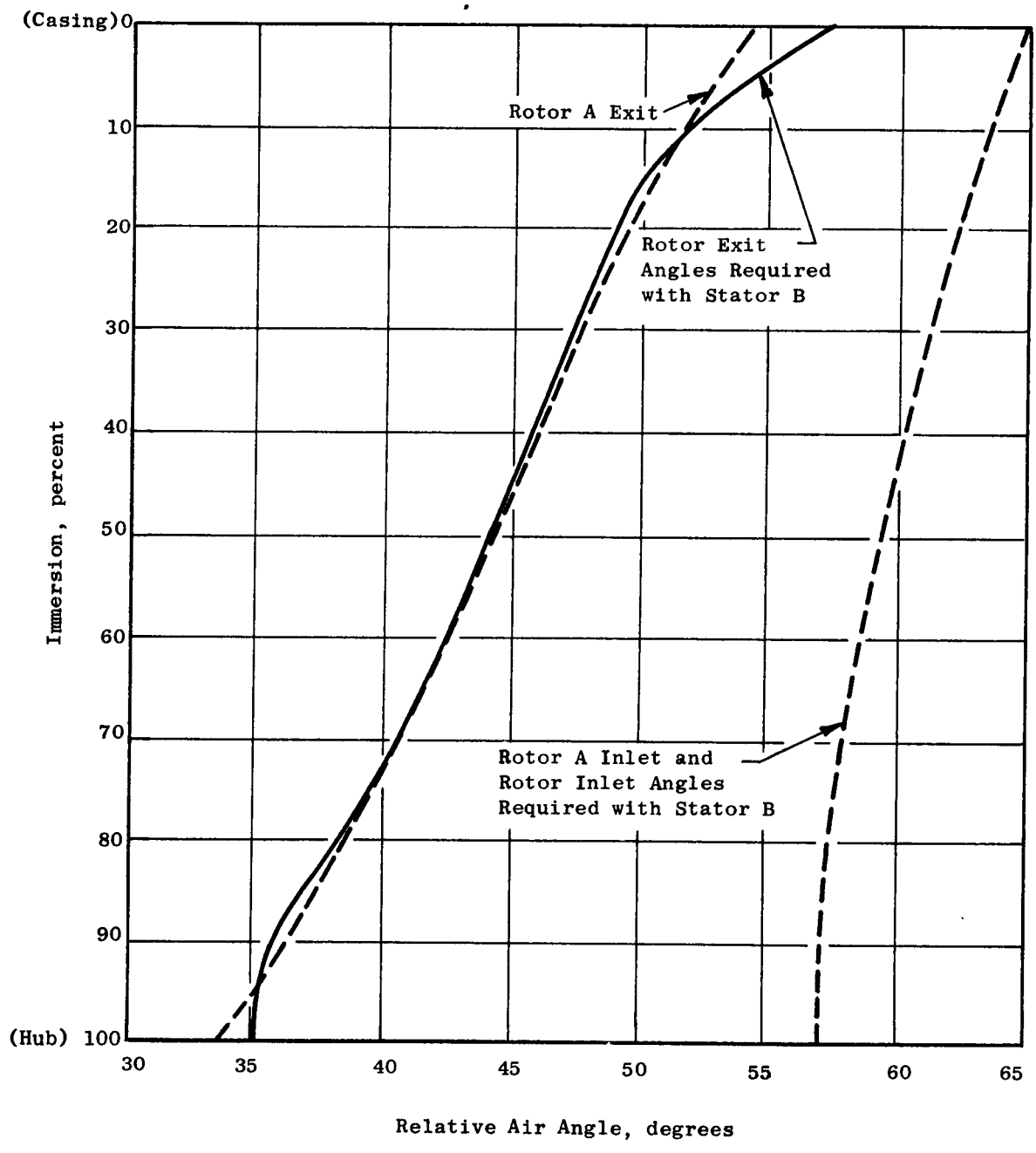

Figure 10. Comparison of the Radial Variation of Inlet and Exit Relative Air Angle Requried for Stator A and Stator B.

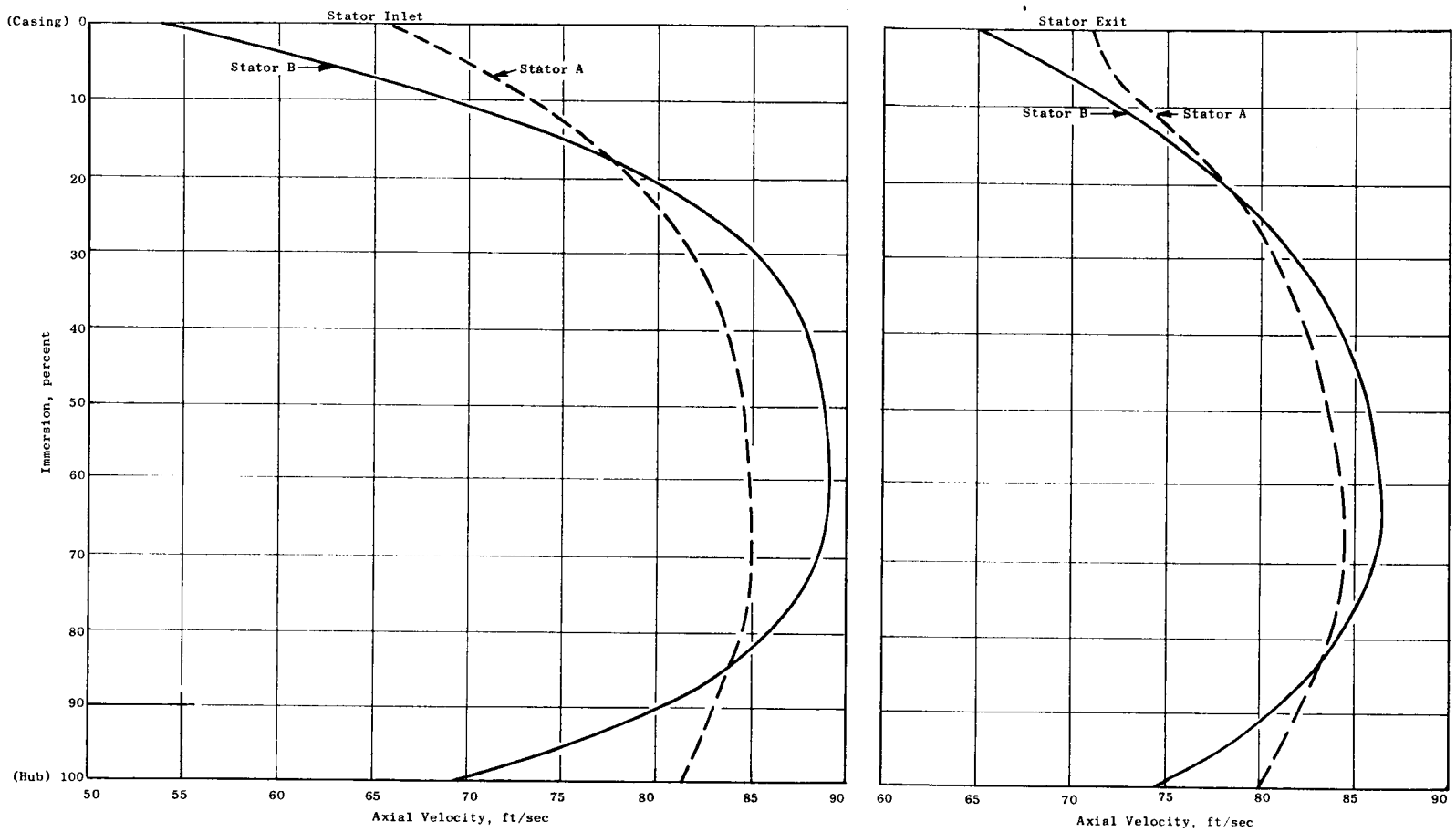

Figure 11. Comparison of the Radial Variation of Axial Velocity for Stator A and Stator B.

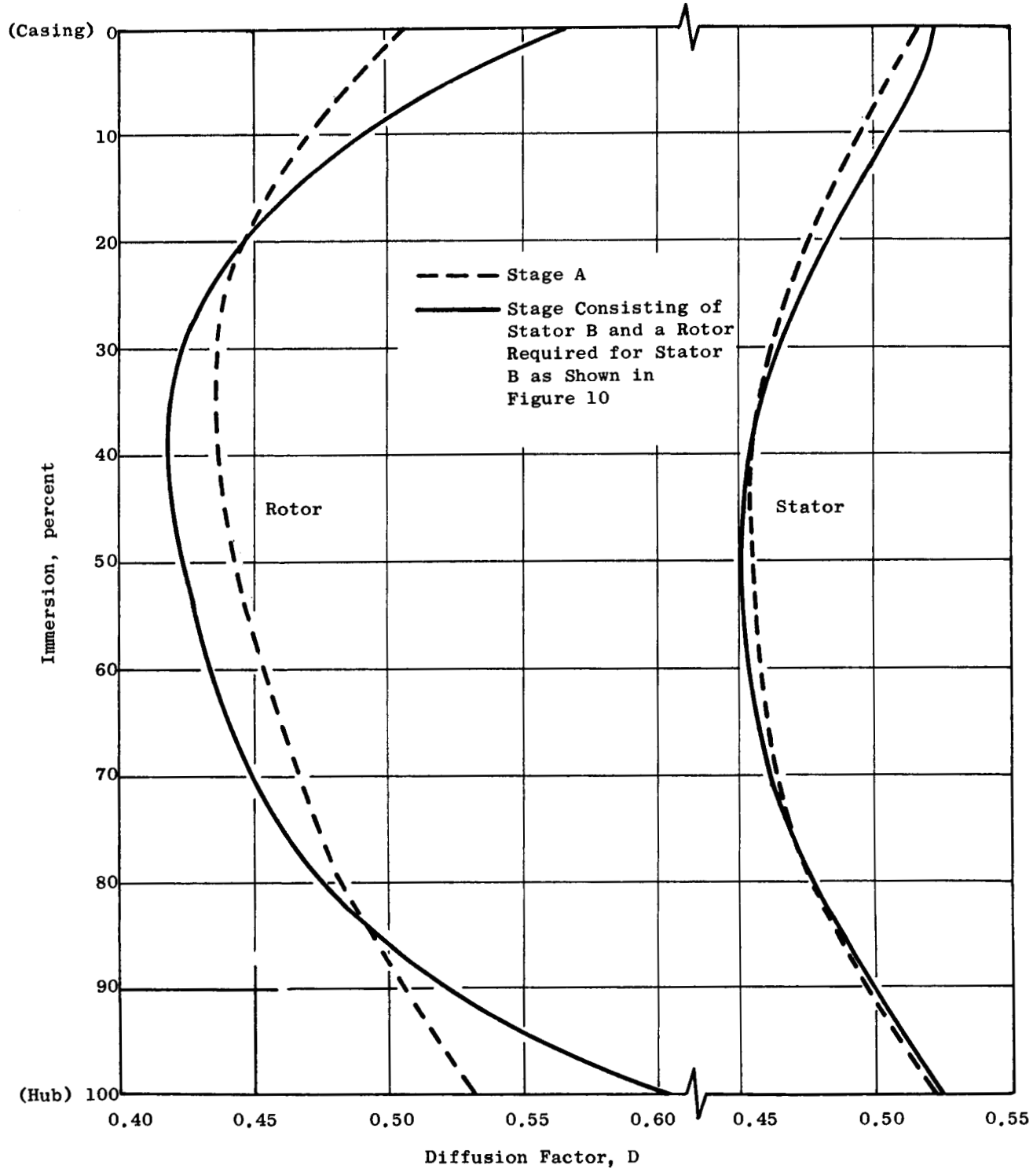

Figure 12. Comparison of Rotor and Stator Diffusion Factor for Stage A and a Stage Consisting of Stator B and a Rotor Required for Stator B as Shown in Figure 10.

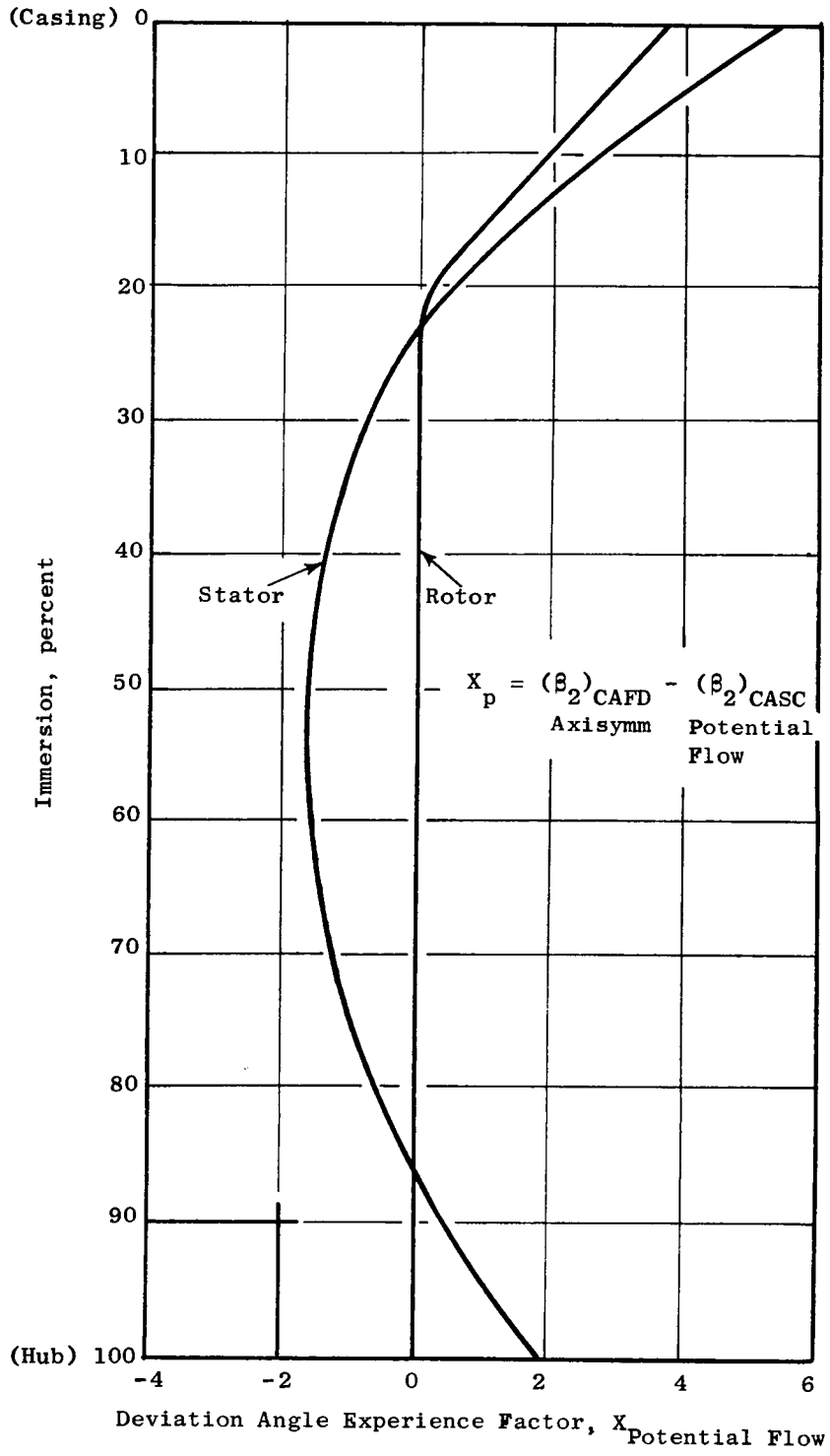

Figure 13. Radial Variation of the Difference Between CAFD and CASC Exit Air Angles for Rotor A and Stator A.

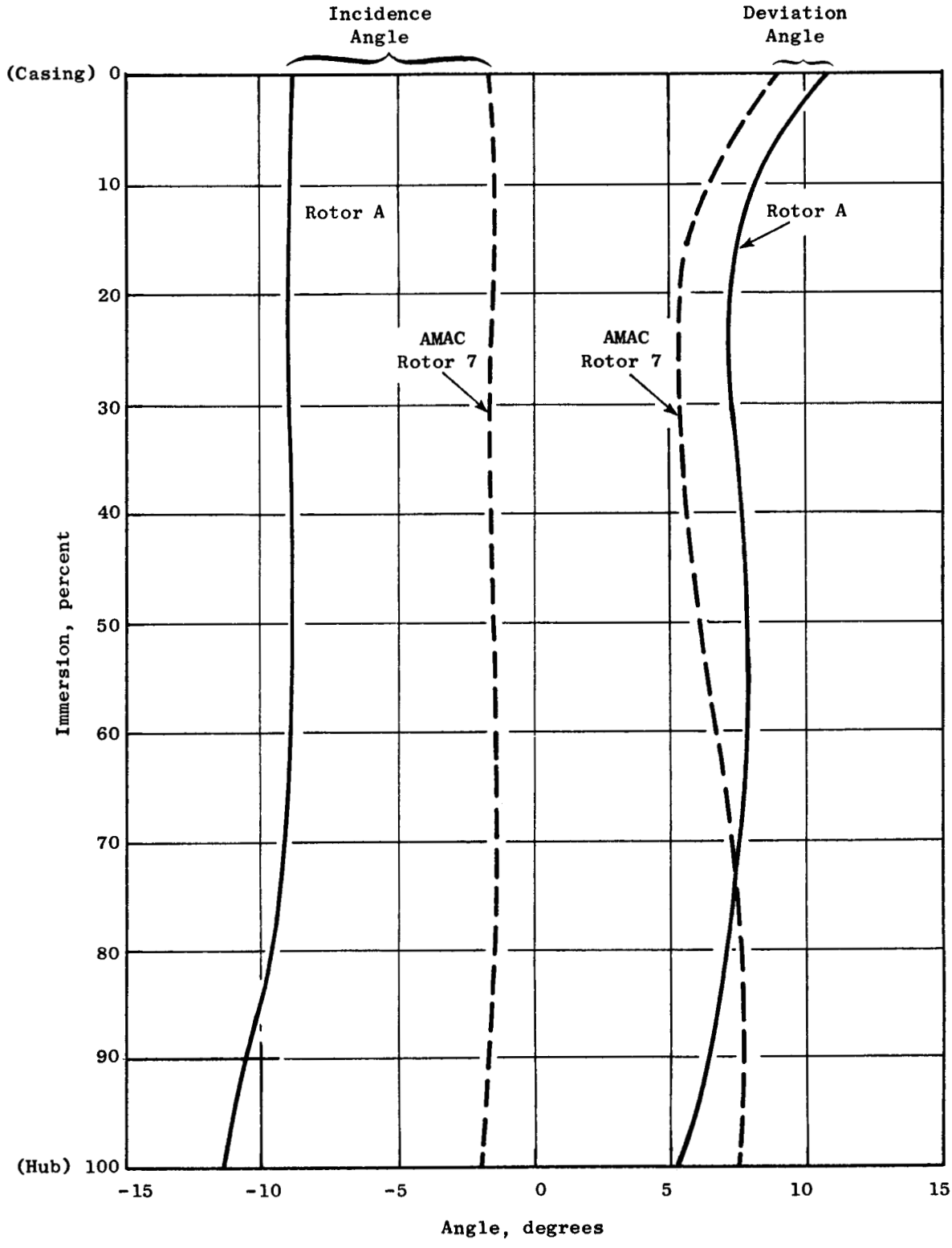

Figure 14. Incidence and Deviation Angle Versus Percent Height for AMAC Rotor 7 and Rotor A.

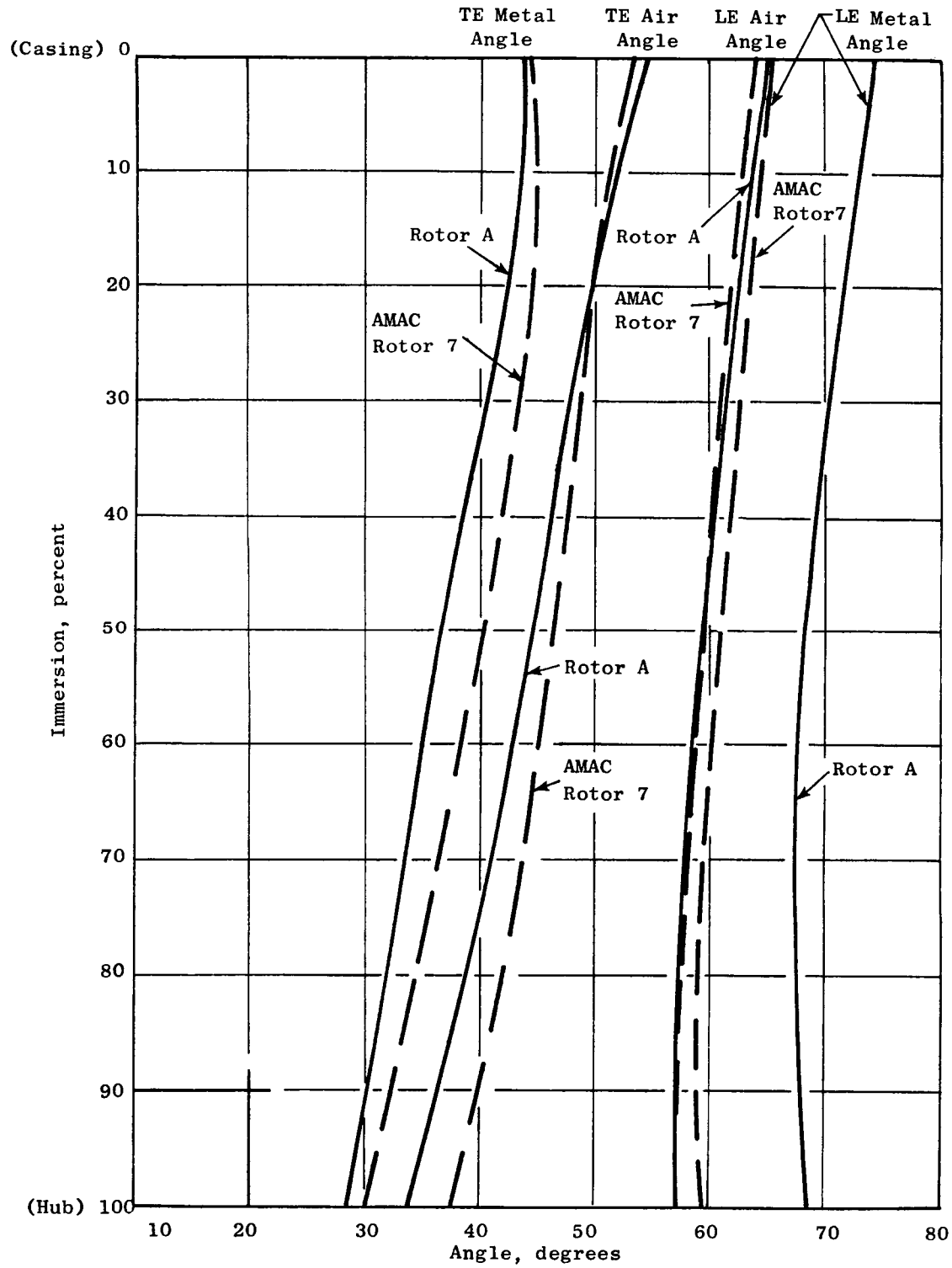

Figure 15. Radial Variation of Relative Air Angles and Leading and Trailing Edge Metal Angles for AMAC Rotor 7 and Rotor A.

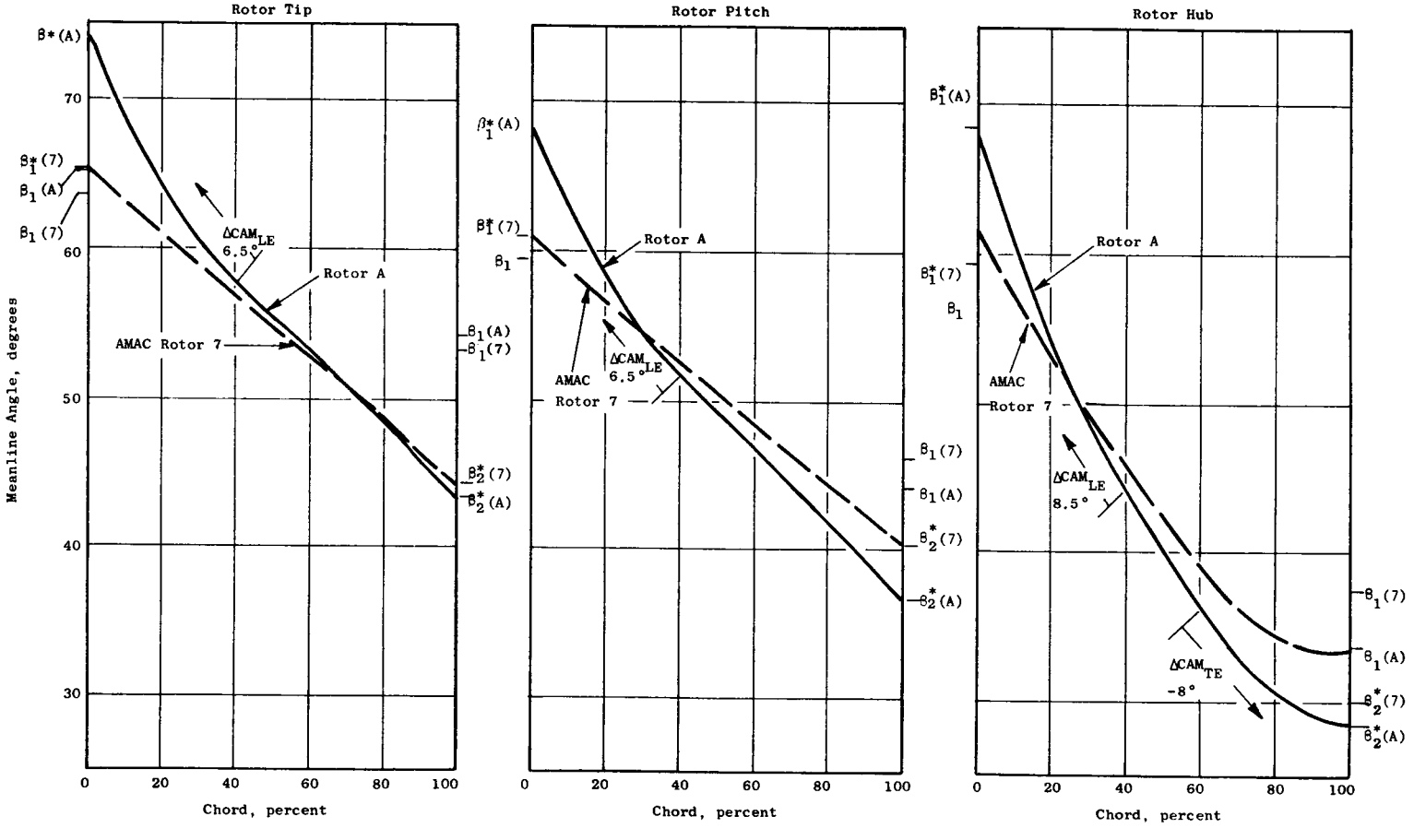

Figure 16. Comparison of Chordwise Variation of Meanline Angle for AMAC Rotor 7 and Rotor A.

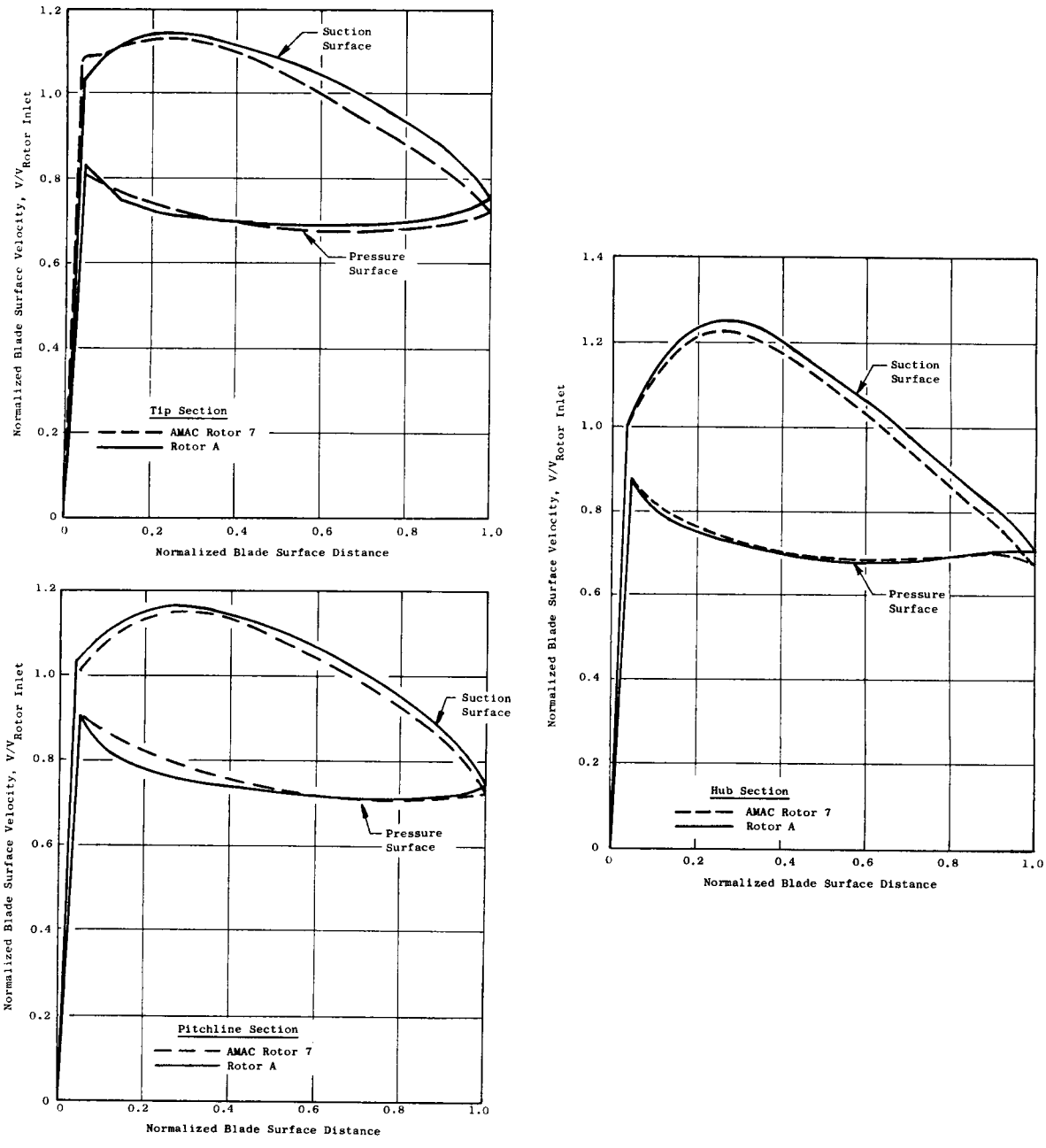

Figure 17. Comparison of the Blade Surface Velocity Distributions for the AMAC Rotor 7 and the Low Speed Rotor A.

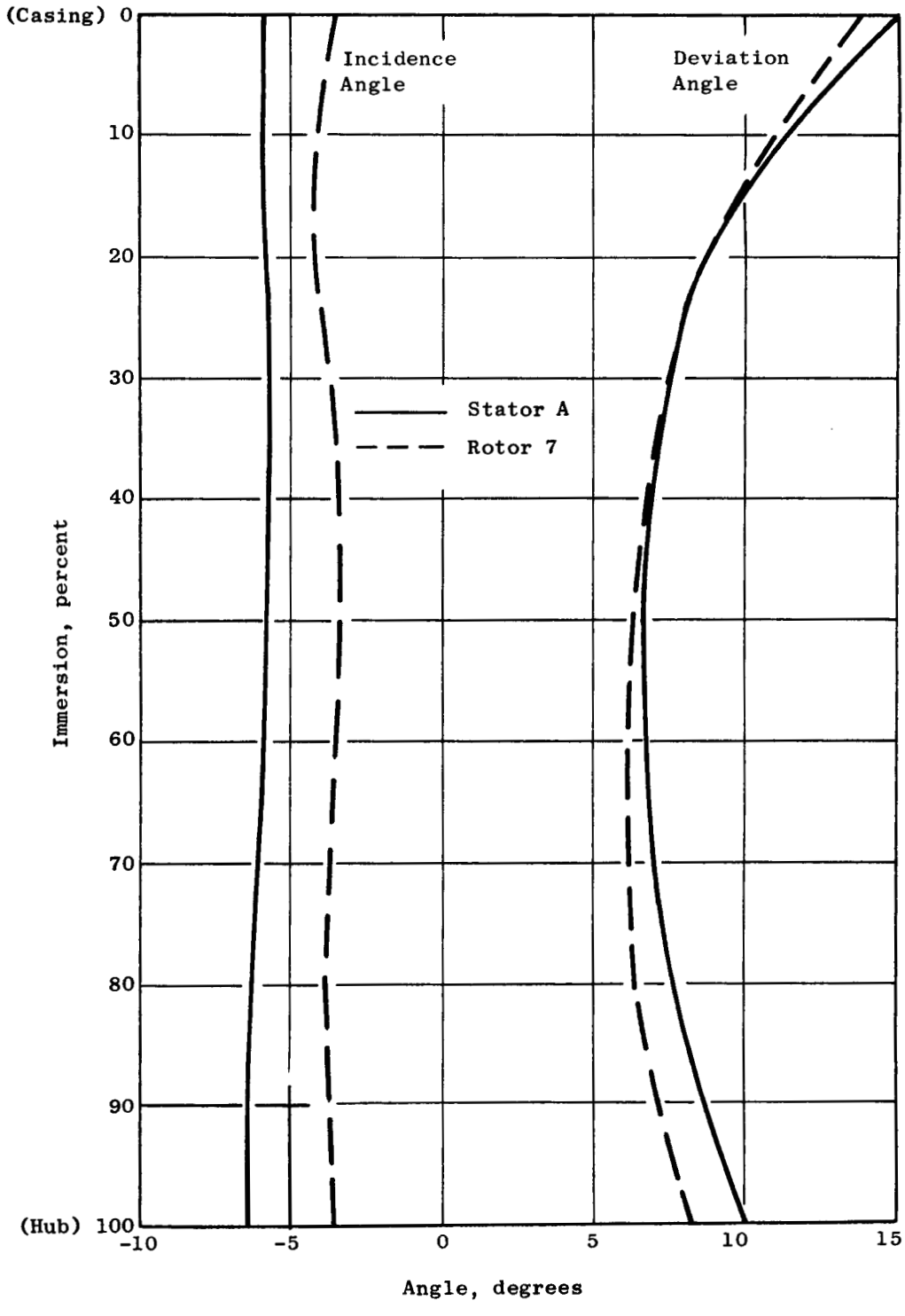

Figure 18. Incidence and Deviation Angle Versus Radius for AMAC Stator 7 and Stator A.

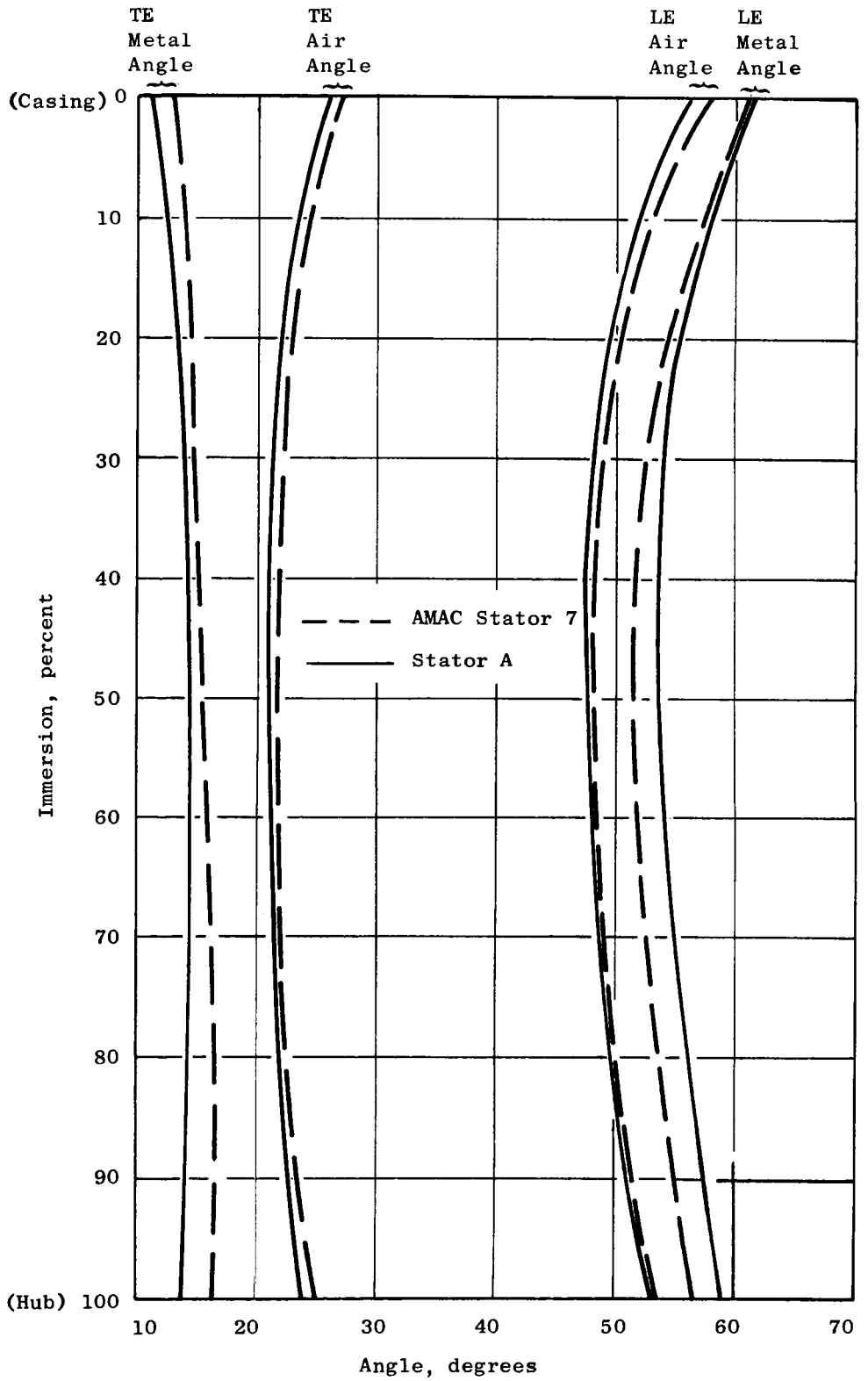

Figure 19. Radial Variation of Absolute Air Angles and Leading and Trailing Edge Metal Angles for AMAC Stator 7 and Stator A.

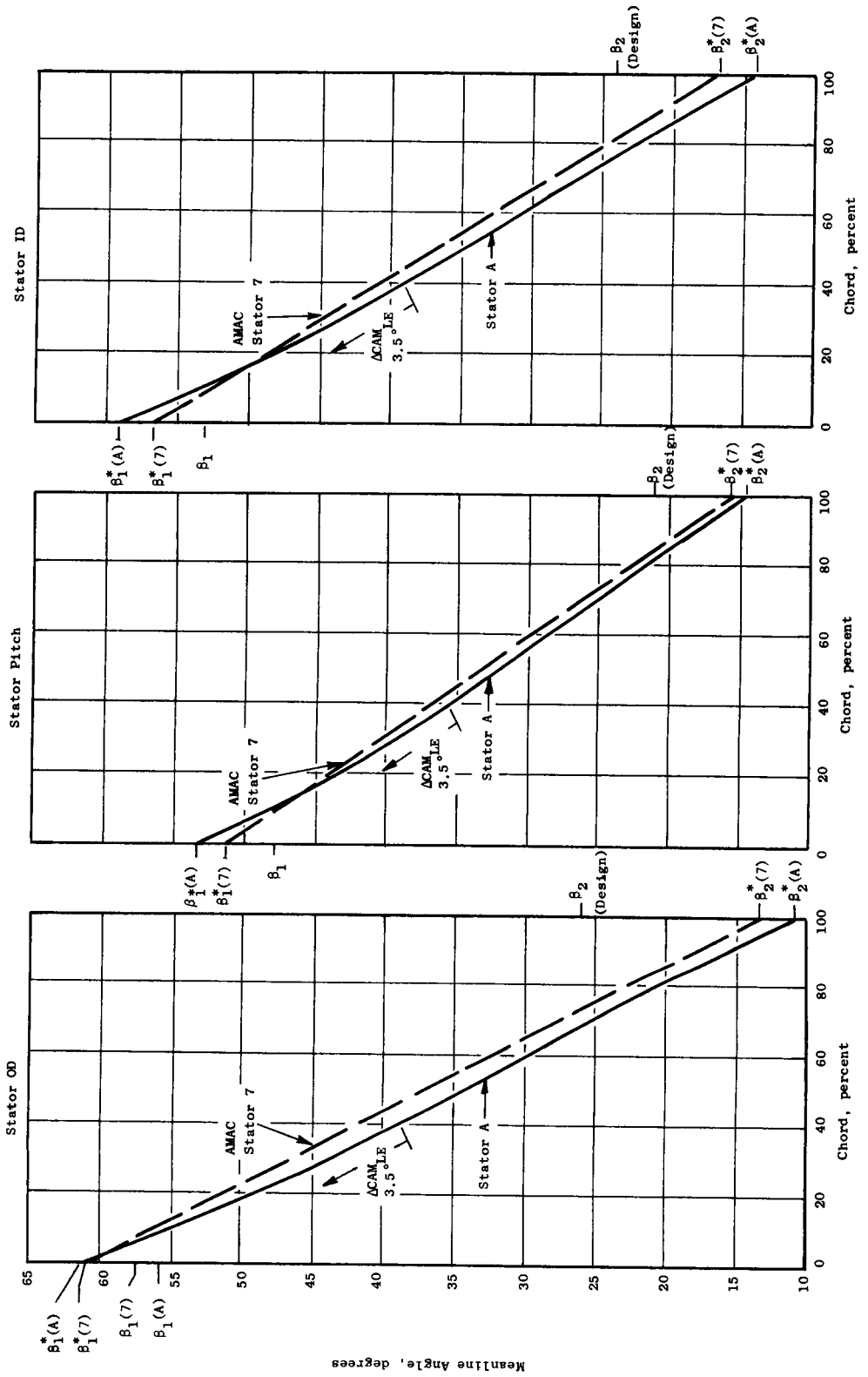

Figure 20. Comparison of Chordwise Variation of Meanline Angle for AMAC Stator 7 and Stator A.

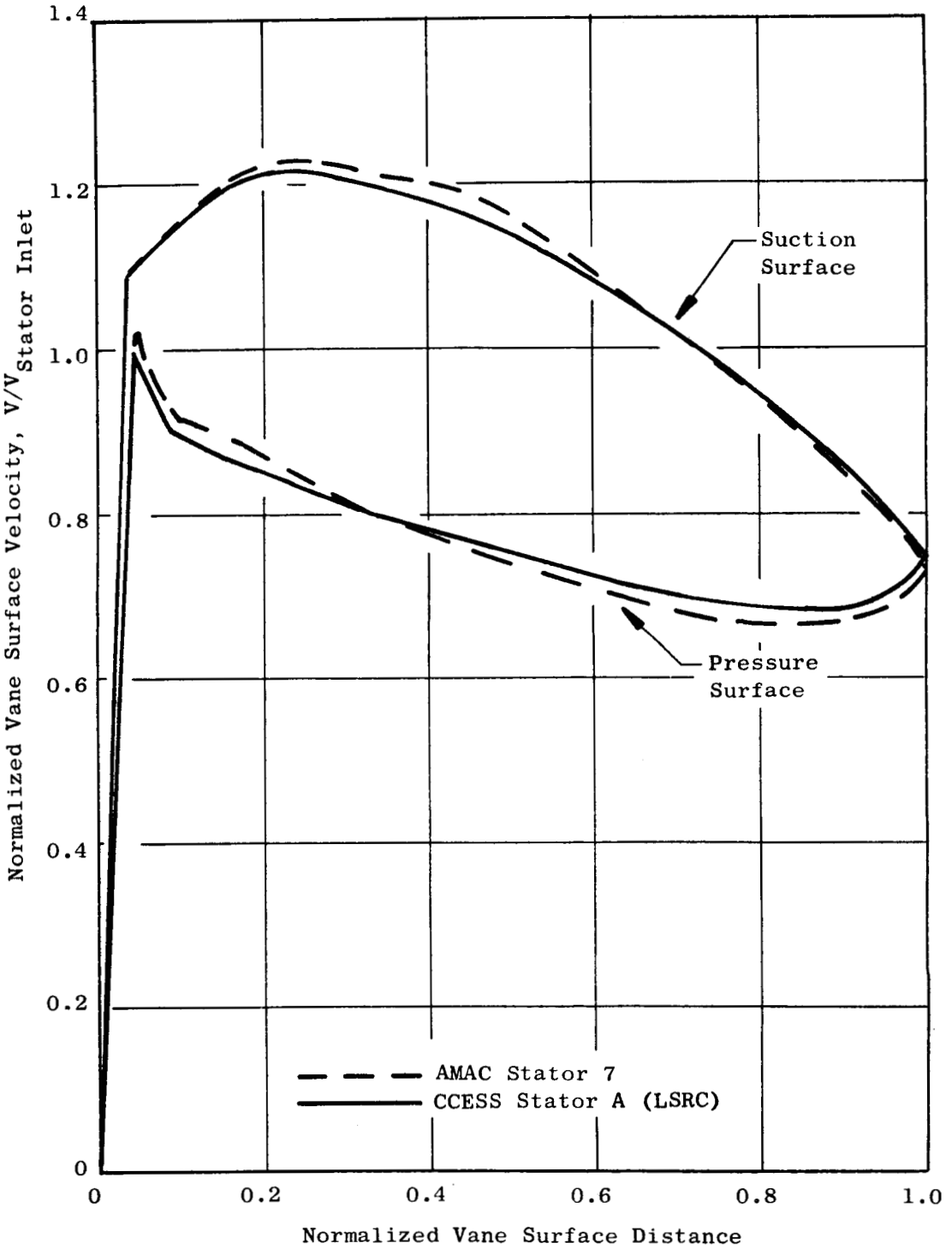

Figure 21. Comparison of the Pitchline Vane Surface Velocity Distributions for the AMAC Stator 7 and the Low Speed Stator A.

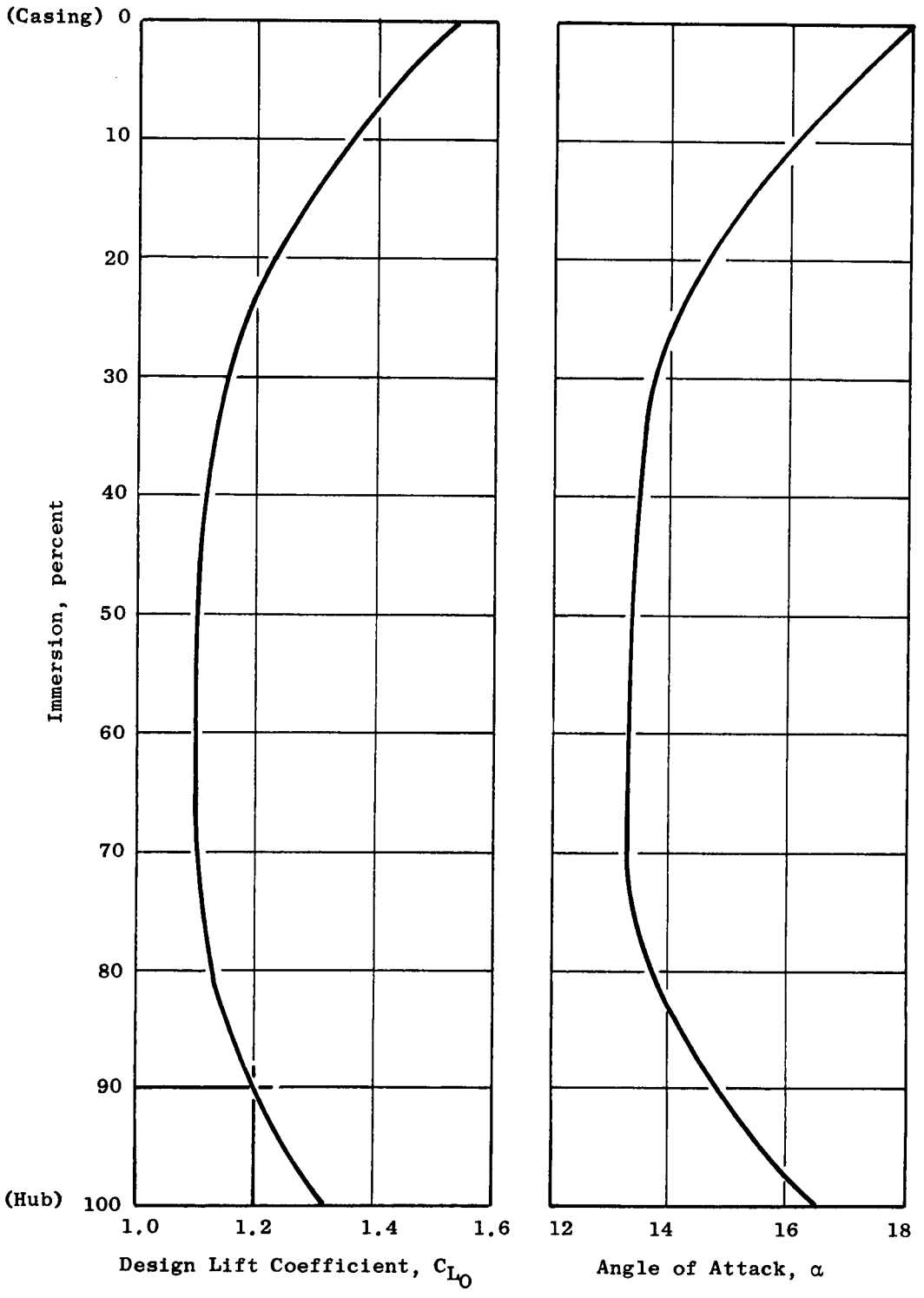

Figure 22. Radial Variation of Design Lift Coefficient and Angle of Attack for the Inlet Guide Vane.

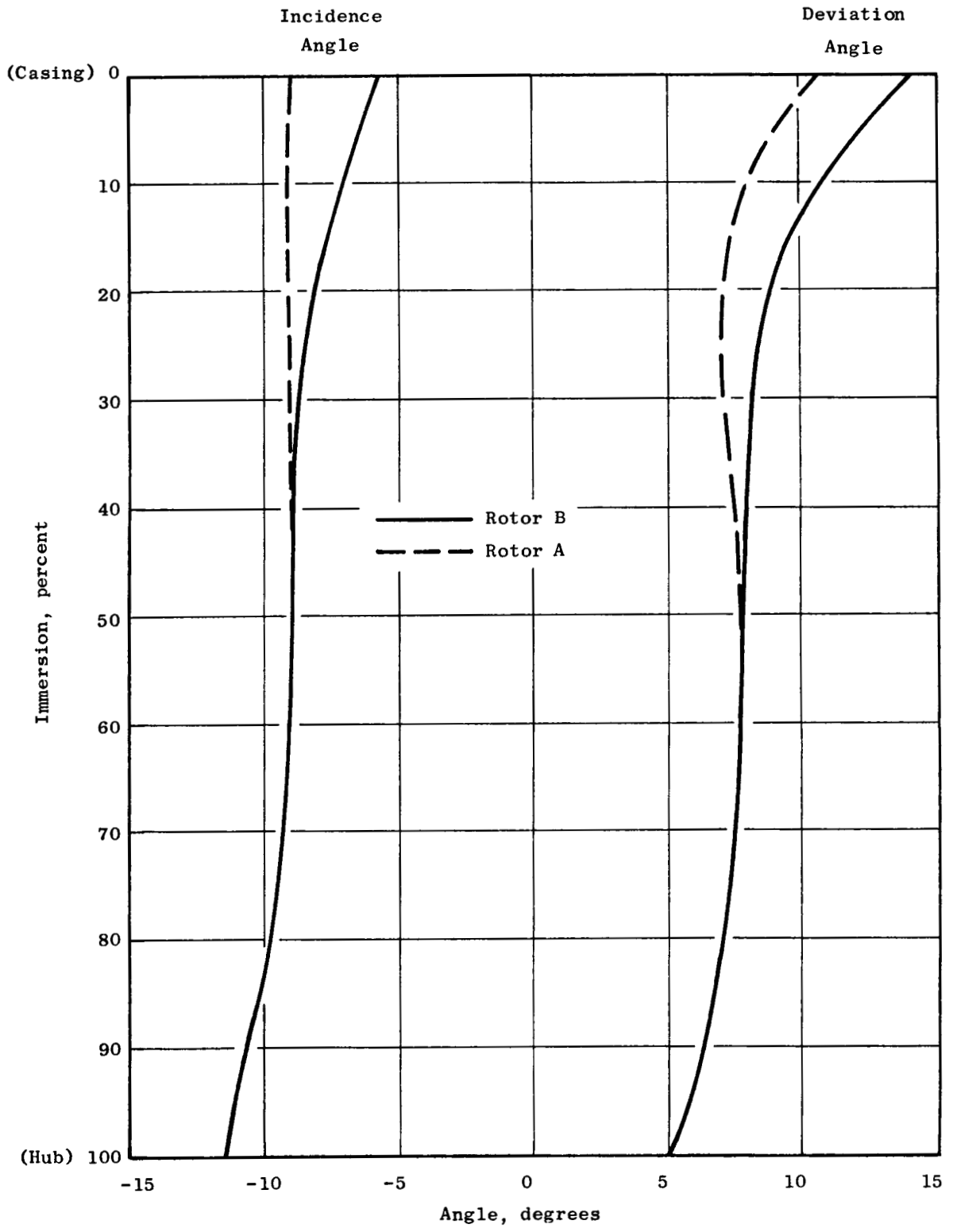

Figure 23. Incidence and Deviation Angle Versus Radius for Rotor B and Rotor A.

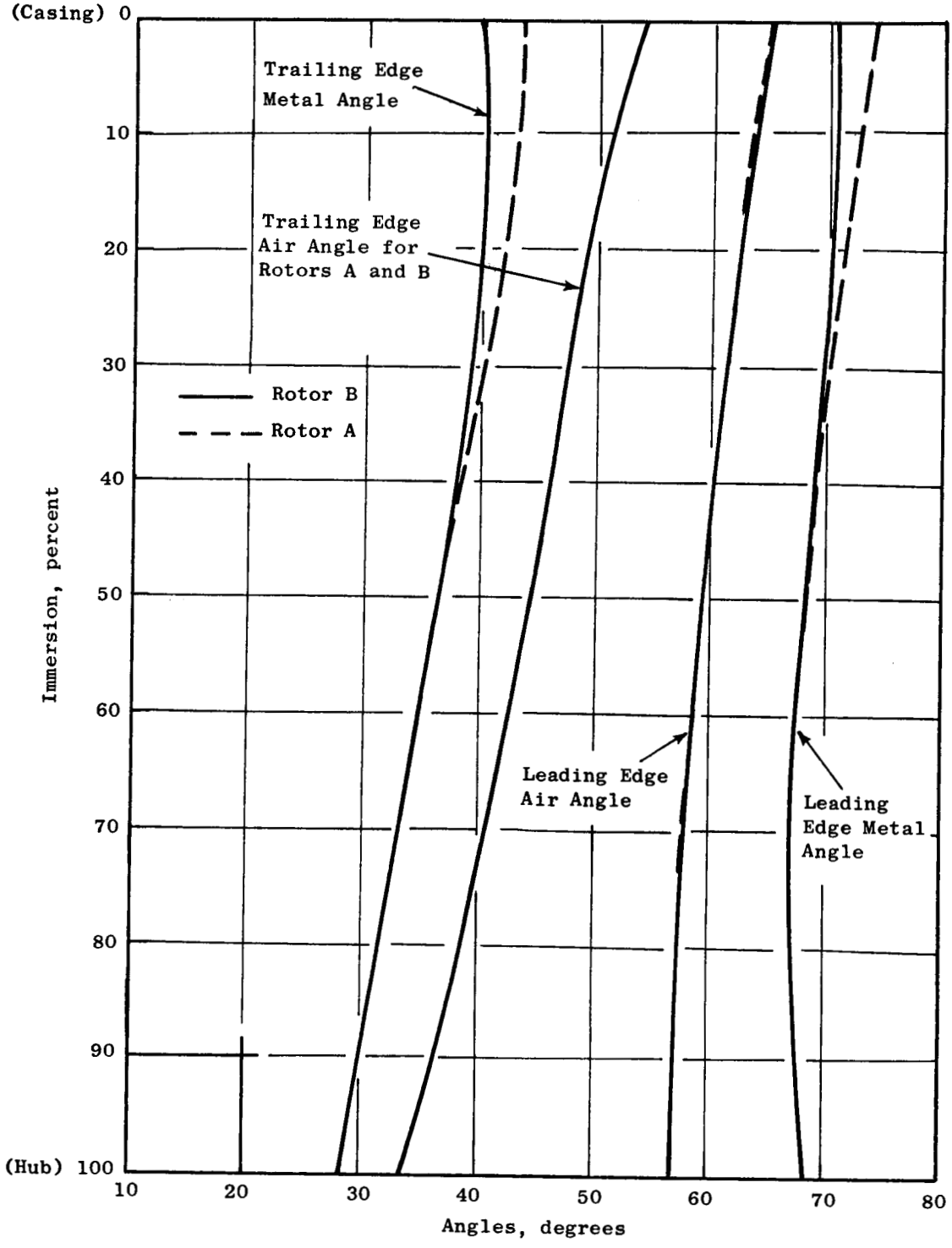

Figure 24. Radial Variation of Relative Air Angles and Leading and Trailing Edge Metal Angles for Rotor B and Rotor A.

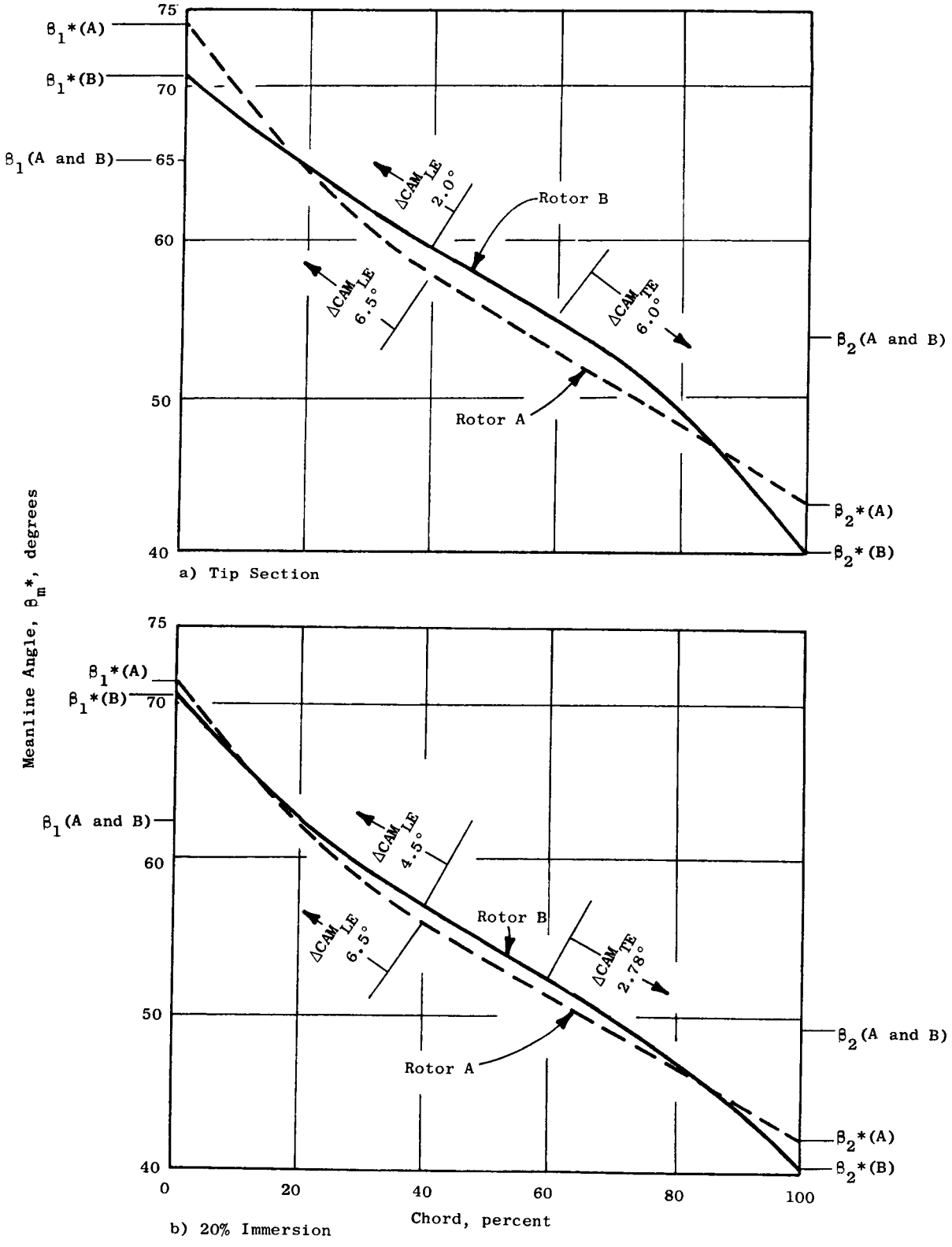

Figure 25. Comparison of the Chordwise Variation of Rotor A and Rotor B Meanline Angles for 0% and 20% Radial Immersion from the Casing.

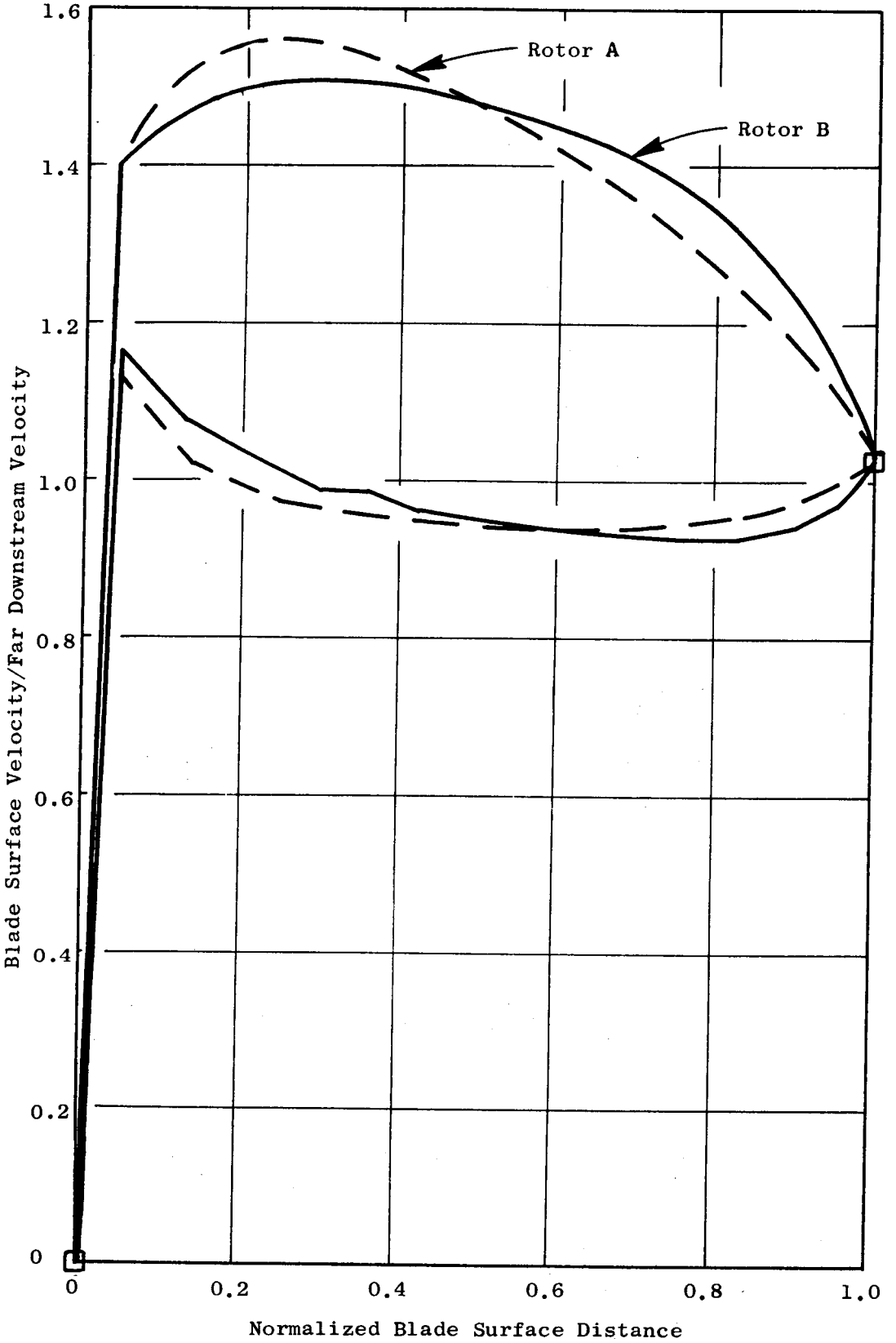

Figure 26. Comparison of the Blade Surface Velocity Distributions for Rotor B and Rotor A Tip Sections.

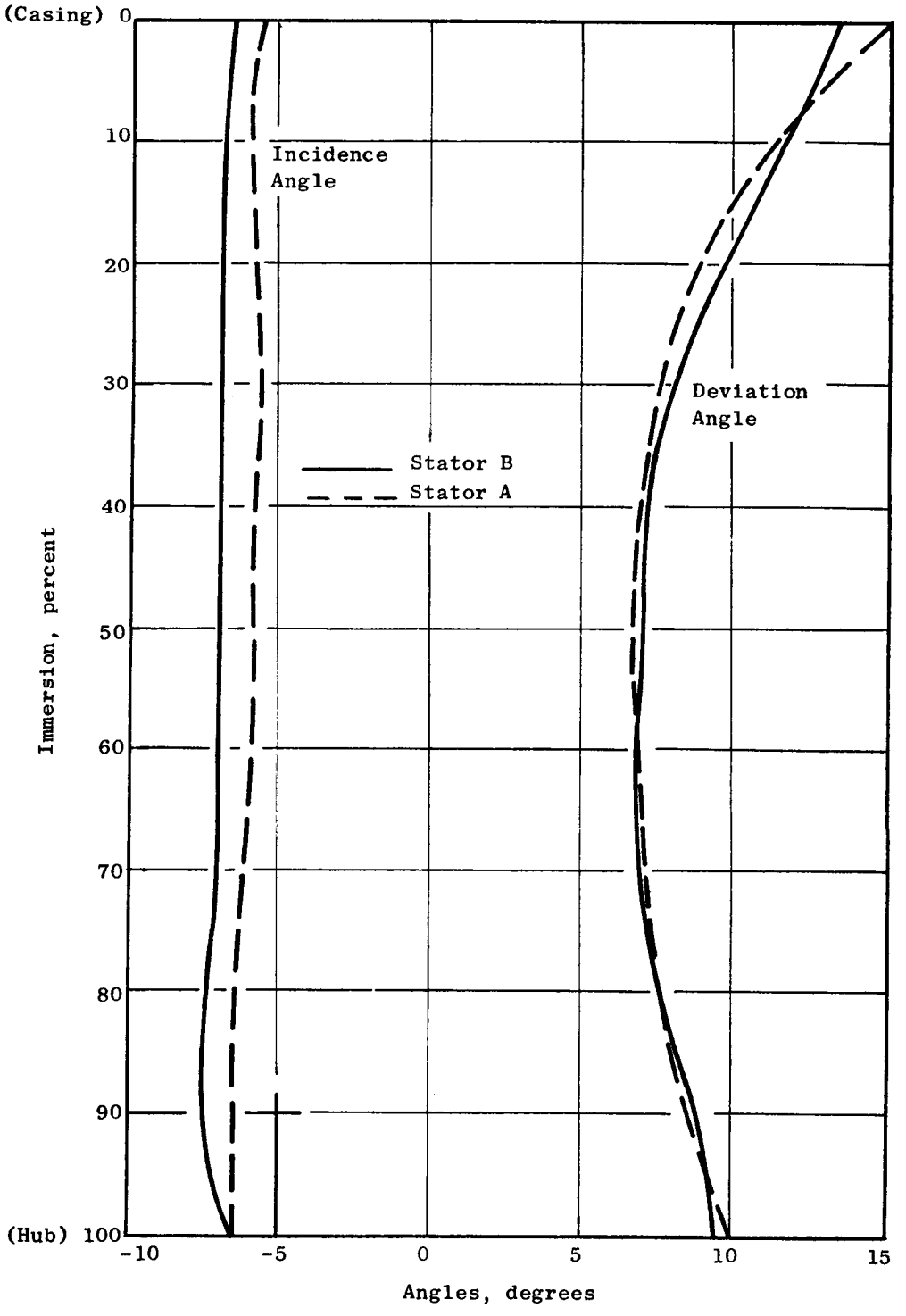

Figure 27. Incidence and Deviation Angle Versus Radius for Stator B and Stator A.

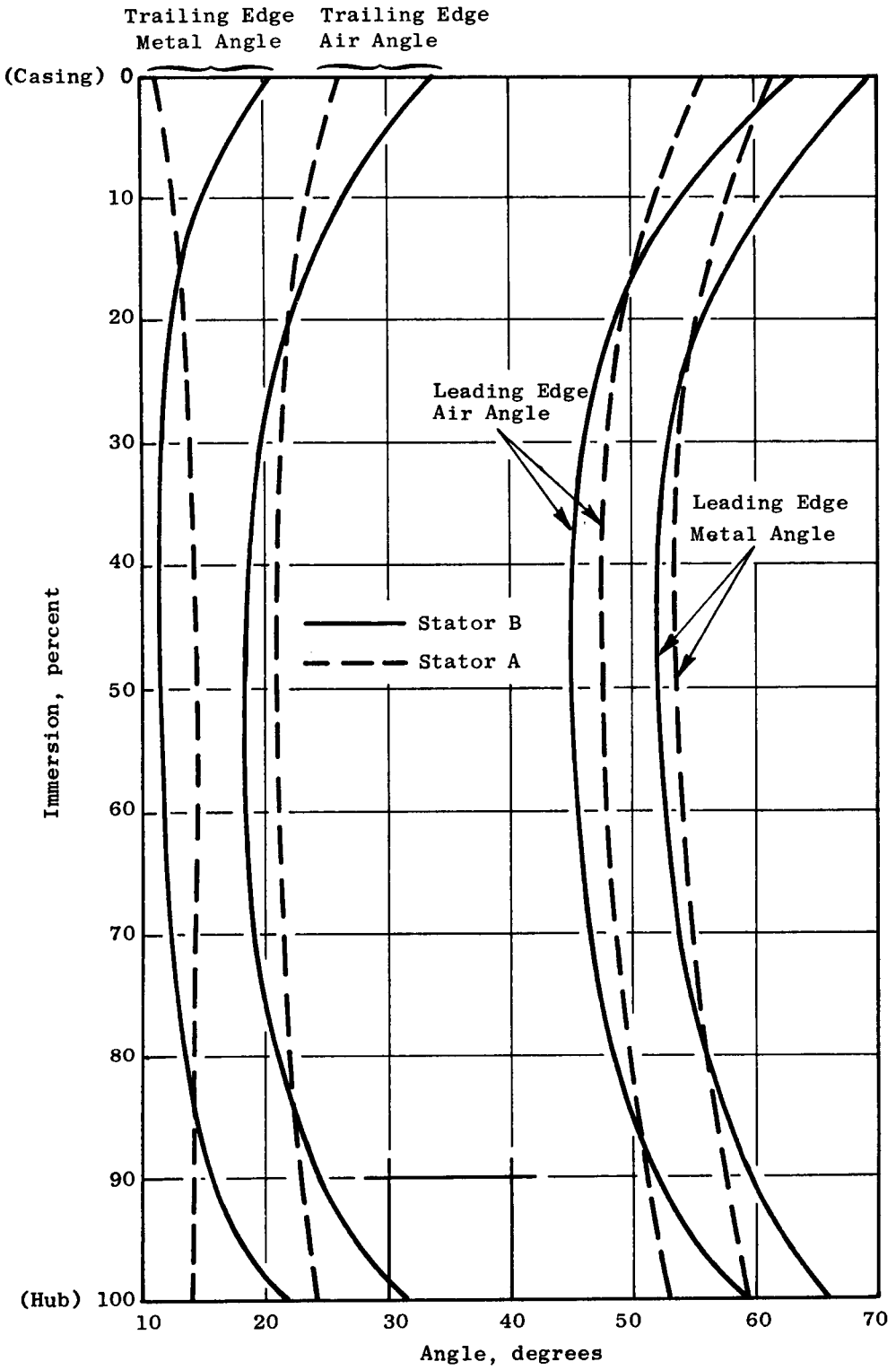

Figure 28. Radial Variation of Absolute Air Angles and Leading and Trailing Edge Metal Angles for Stator B and Stator A.

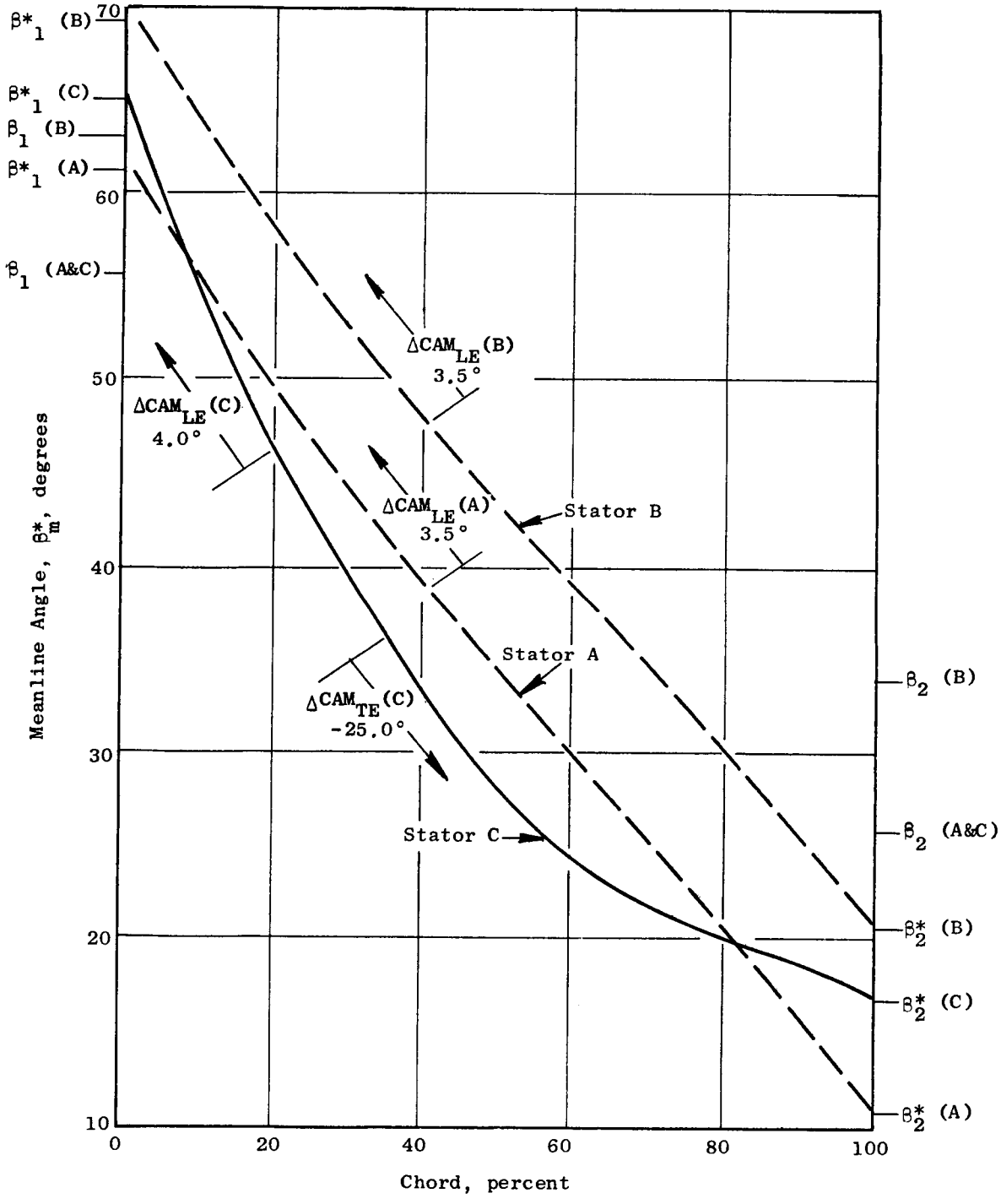

Figure 29. Comparison of Chordwise Variation of Meanline Angle for Stator A, Stator B and Stator C Vane Sections at the Outer Diameter.

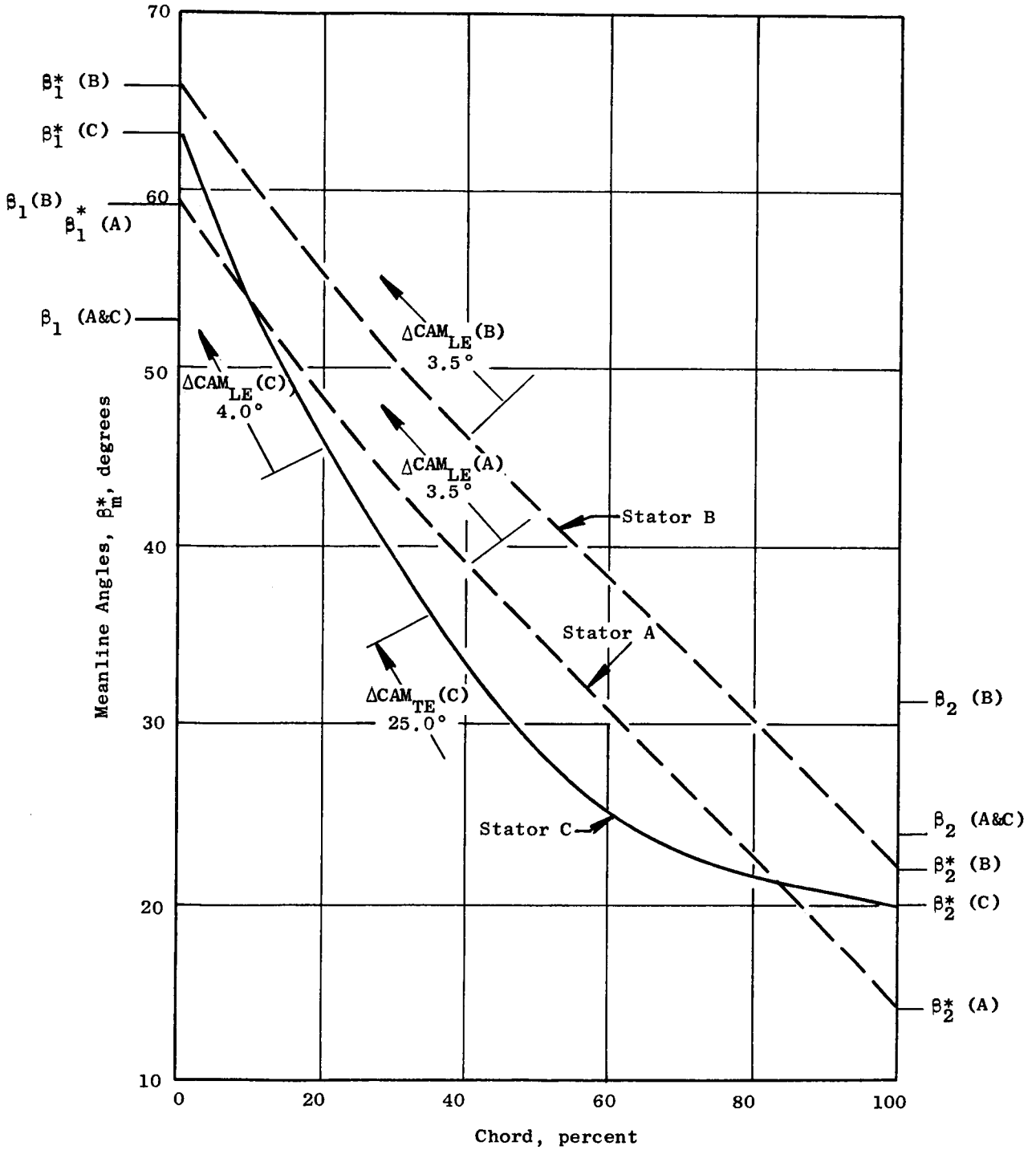

Figure 30. Comparison of Chordwise Variation of Meanline Angle for Stator A, Stator B and Stator C Vane Sections at the Inner Diameter.

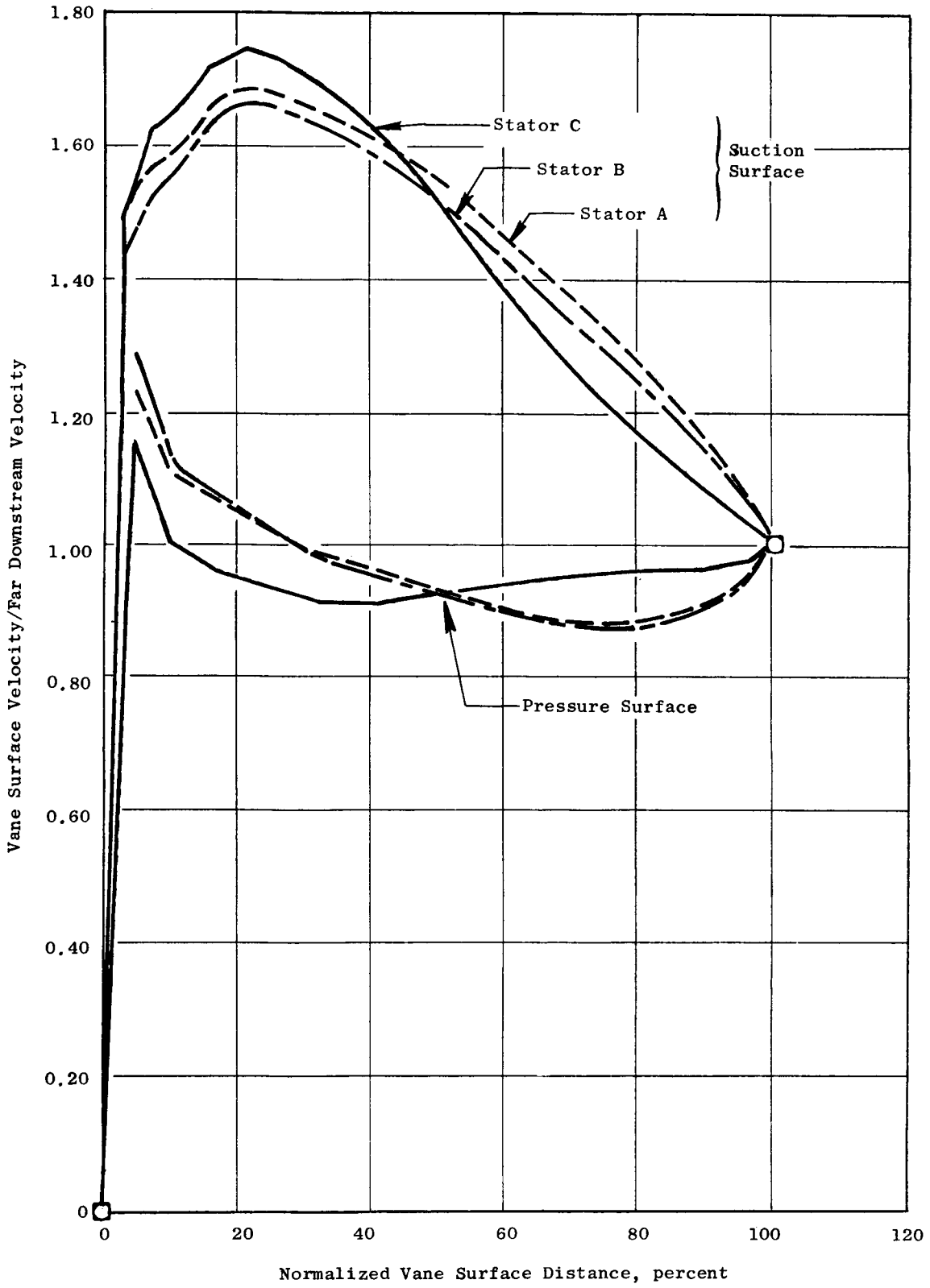

Figure 31. Comparison of Vane Surface Velocity Distributions for Stator A, Stator B and Stator C Sections at the Outer Diameter.

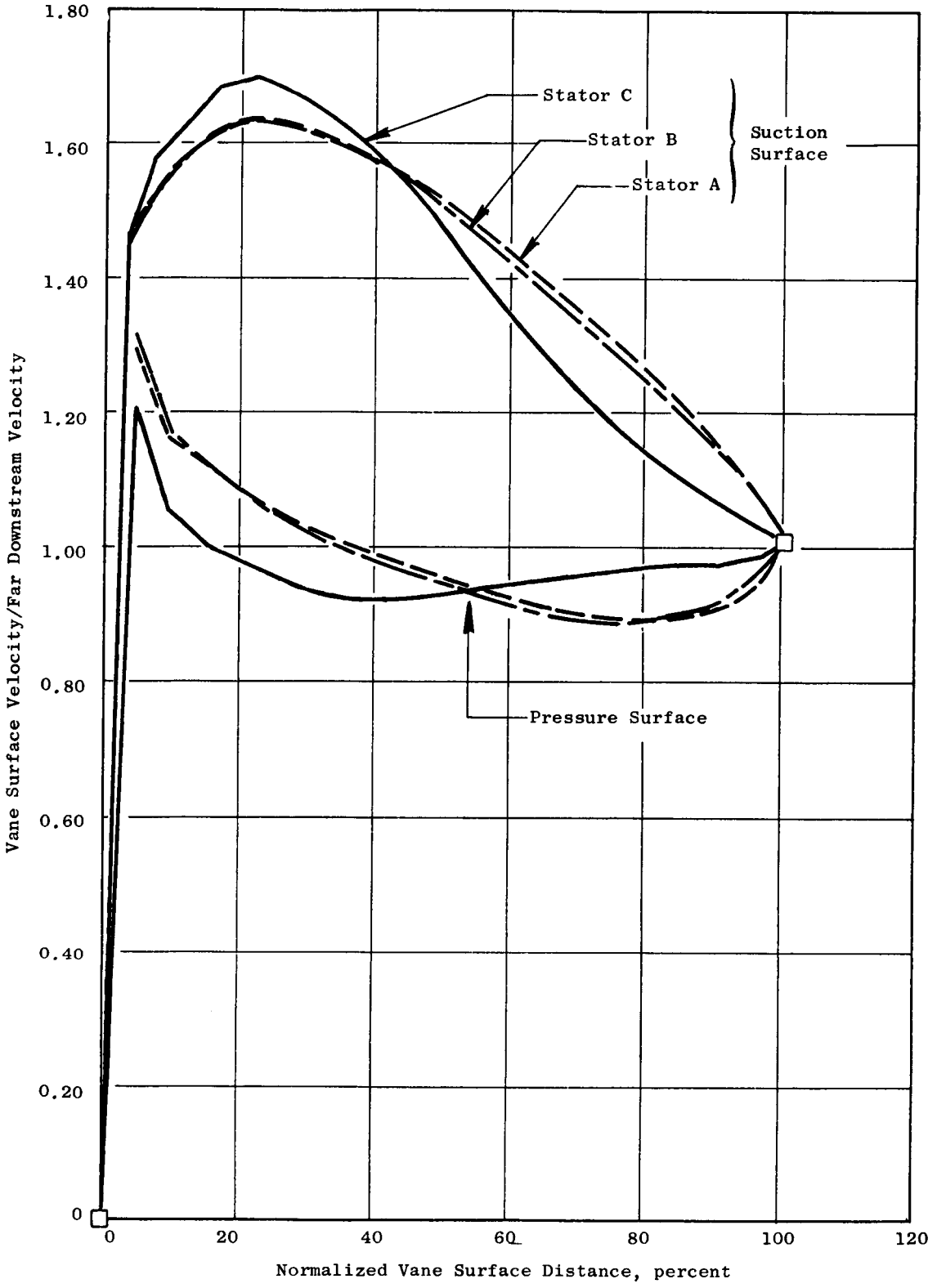

Figure 32. Comparison of Vane Surface Velocity Distributions for Stator A, Stator B and Stator C Stations at the Inner Diameter.

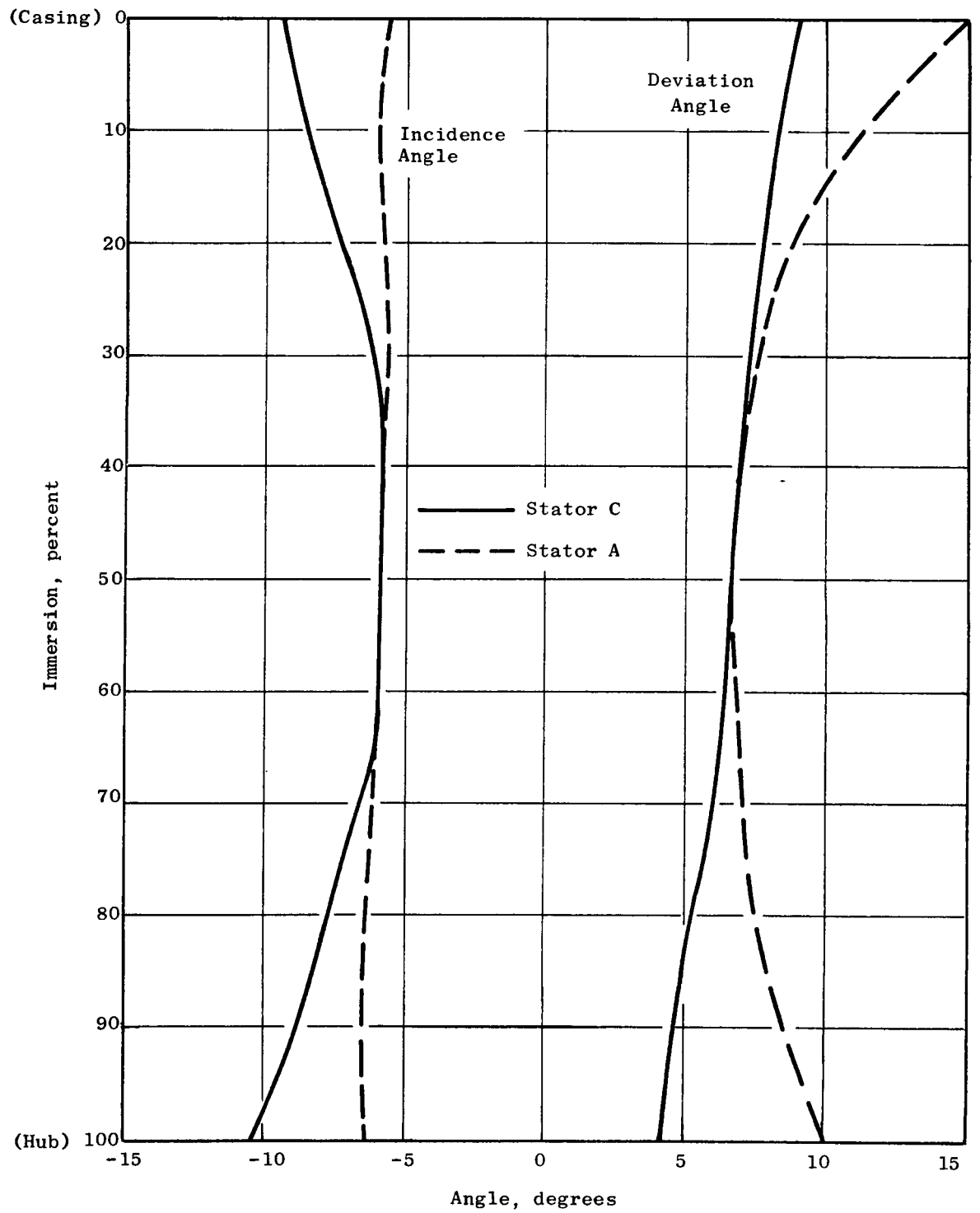

Figure 33. Incidence and Deviation Angle Versus Radius for Stator C and Stator A.

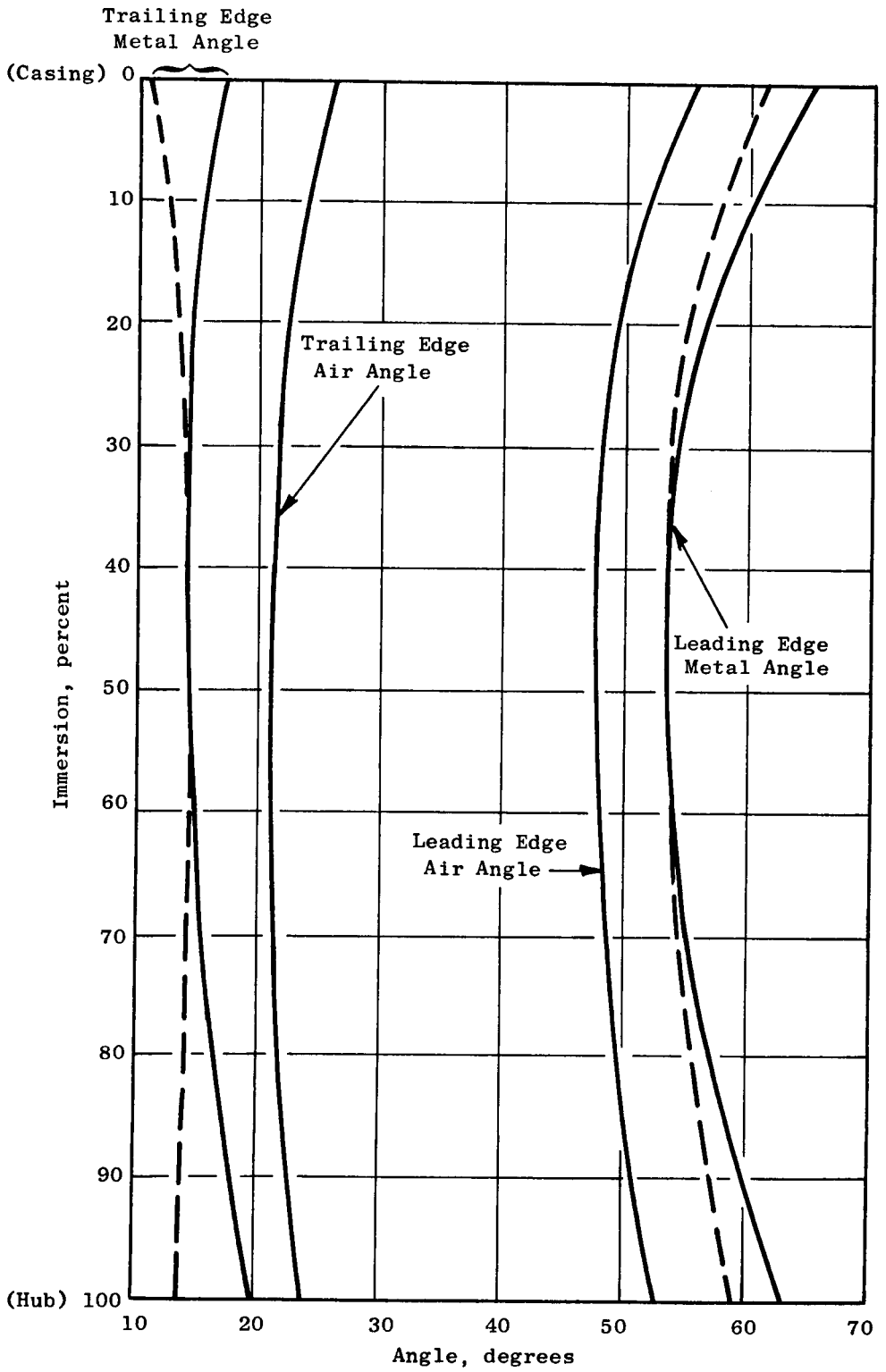

Fi-ure 34. Radial Variation of Relative Air Angles and Leading and Trailing Edge Metal Angles for Stator C and Stator A.